This article was downloaded by:
On: *21 January 2011*
Access details: *Access Details: Free Access*
Publisher *Taylor & Francis*
Informa Ltd Registered in England and Wales Registered Number: 1072954 Registered office: Mortimer House, 37-41 Mortimer Street, London W1T 3JH, UK

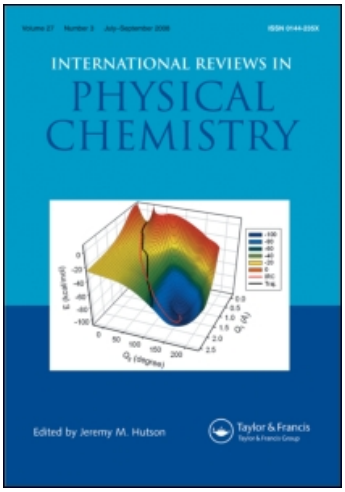

International Reviews in Physical Chemistry
Publication details, including instructions for authors and subscription information:
http://www.informaworld.com/smpp/title~content=t713724383

Molecular, multiresonant coherent four-wave mixing spectroscopy

John C. Wright[a]; Roger J. Carlson[ab]; Gregory B. Hurst[ac]; John K. Steehler[ad]; Michael T. Riebe[ae]; Bradford B. Price[af]; Dinh C. Nguyen[ab]; Steven H. Lee[ag]
[a] Department of Chemistry, University of Wisconsin-Madison, Madison, WI, USA [b] Los Alamos National Laboratory, Los Alamos, NM [c] Oak Ridge National Laboratories, Oak Ridge, TN [d] Roanoke College, Salem, VA [e] Glaxo, Inc., NC [f] Proctor and Gamble Corp., Cincinnati, OH [g] Walla Walla College, College Place, WA, USA

To cite this Article Wright, John C. , Carlson, Roger J. , Hurst, Gregory B. , Steehler, John K. , Riebe, Michael T. , Price, Bradford B. , Nguyen, Dinh C. and Lee, Steven H.(1991) 'Molecular, multiresonant coherent four-wave mixing spectroscopy', International Reviews in Physical Chemistry, 10: 4, 349 — 390
To link to this Article: DOI: 10.1080/01442359109353262
URL: http://dx.doi.org/10.1080/01442359109353262

PLEASE SCROLL DOWN FOR ARTICLE

Full terms and conditions of use: http://www.informaworld.com/terms-and-conditions-of-access.pdf

This article may be used for research, teaching and private study purposes. Any substantial or systematic reproduction, re-distribution, re-selling, loan or sub-licensing, systematic supply or distribution in any form to anyone is expressly forbidden.

The publisher does not give any warranty express or implied or make any representation that the contents will be complete or accurate or up to date. The accuracy of any instructions, formulae and drug doses should be independently verified with primary sources. The publisher shall not be liable for any loss, actions, claims, proceedings, demand or costs or damages whatsoever or howsoever caused arising directly or indirectly in connection with or arising out of the use of this material.

INTERNATIONAL REVIEWS IN PHYSICAL CHEMISTRY, 1991, VOL. 10, NO. 4, 349–390

Molecular, multiresonant coherent four-wave mixing spectroscopy†

by JOHN C. WRIGHT, ROGER J. CARLSON, GREGORY B. HURST, JOHN K. STEEHLER, MICHAEL T. RIEBE, BRADFORD B. PRICE, DINH C. NGUYEN and STEVEN H. LEE

Department of Chemistry, University of Wisconsin–Madison, Madison, WI 53706, USA

Recent research has expanded the capabilities of four-wave mixing by providing it with component selectivity, site selectivity, and mode selectivity. The selectivity is achieved by taking advantage of the three resonance enhancements that occur in a four-wave mixing process. New spectral scanning strategies allow one to scan a single resonance while maintaining the other two resonances at constant values. The constant resonances can be used to select a specific component, a specific site within an inhomogeneously broadened envelope of a component, and/or a specific vibrational or vibronic mode of that site. The scanned resonance will then contain enhanced features corresponding to the particular component, site, and/or mode that was chosen by the constant resonances. These component and site selective capabilities of the four-wave mixing complement the single vibronic level fluorescence methods. The relative transition intensities from a specific component or site reflect the mode coupling between the vibrational and vibronic modes. Since the four-wave mixing is fully resonant in these experiments, saturation effects play a dominant role and cannot be ignored. This review presents a complete discussion of the theoretical and experimental factors that control the fully resonant four-wave mixing. It shows examples of the component selectivity and the line narrowing capabilities. It also provides examples of how mode selection can identify mode coupling through the relative intensities of different vibrational features.

Downloaded At: 17:36 21 January 2011

1. Introduction

1.1. *Background*

The potential for using coherent four-wave mixing (CFWM) for molecular spectroscopy was first demonstrated in the pioneering coherent anti-Stokes Raman scattering (CARS) experiments of Begley, Harvey and Byer [1]. There was initially great excitement about these methods because they produced a coherent, sharply-defined beam of light at the Raman frequency that was actually visible to the eye. These results were startling because spontaneous Raman emission is usually such a weak process that one cannot perform Raman experiments at particulary low concentration levels. An entire fleet of CFWM methods followed that extended the capabilities of CARS and provided new insights into the factors controlling the mixing process [2–10]. Unfortunately, it soon became apparent that CARS was limited by a nonresonant

† This work was supported by the National Science Foundation under grants CHE-8903556 and CHE-8515692.

Present addresses: R. J. Carlson and D. C. Nguyen are at Los Alamos National Laboratory, Los Alamos, NM 87545; G. B. Hurst is at Oak Ridge National Laboratories, Oak Ridge, TN 37932; J. K. Steehler is at Roanoke College, Salem, VA 24153; M. T. Riebe is at Glaxo, Inc., Research Triangle Park, NC 27709; B. B. Price is at Proctor and Gamble Corp., Cincinnati, OH; and S. H. Lee is at Walla Walla College, College Place, WA 99324, U.S.A..

0144-235X/91 $3·00 © 1991 Taylor & Francis Ltd.

background, and in general, CFWM methods (in their common implementations) had detection limits quite similar to common old ordinary Raman spectroscopy (COORS) [7, 8]. Nevertheless, CARS has some unique capabilities that have given it a home among molecular spectroscopic methods [11, 12]. Its coherence and its capability for spatial and temporal resolution have been particularly important for obtaining vibrationally resolved spectra in fluorescent samples and in hostile environments [13].

Recent research has focused on multiresonant CFWM as a means of achieving new spectroscopic capabilities [14, 22]. In particular, CFWM differs from most conventional spectroscopies in that the mixing efficiency depends upon three simultaneous and potentially different resonances. In this sense, the very nature of a CFWM spectrum depends strongly on the choice of resonances.

This review describes research directed toward using the multiple resonances to achieve spectral selectivity of a variety and magnitude not achievable by traditional methods. In this methodology, one resonance is assigned the task of spectrally selecting a component within a sample or a site within an inhomogeneously broadened band. A second resonance then selects a vibrational or vibronic (i.e. vibrational levels of the electronically excited state) normal mode, and the third resonance is scanned to provide a spectrum of the component (or site) and mode that were chosen by the first two resonances. The resulting spectra are both component and mode selective and vary dramatically as one changes the first two resonances to accent different components and modes.

Downloaded At: 17:36 21 January 2011

The selectivity capabilities of multiresonant CFWM have clear analogs in other laser spectroscopies. Site selective, laser-induced fluorescence is a well-developed technique where an absorption line of a particular sample component is selectively excited and the fluorescence resonances of the selected component are studied [23]. Fluorescence line narrowing is a form of site selective spectroscopy where particular sites within an inhomogeneously broadened band are excited so that sharp-lined fluorescence resonances from those selected sites result [24–27]. In terms of normal mode selectivity, single vibronic level fluorescence spectroscopy is performed by exciting a specific vibronic state and examining the fluorescence transitions of that vibronic state to different vibrational modes [28]. The relative intensities reflect the different couplings between the modes.

The first work in molecular, multiresonant CFWM appeared in a paper by DeCola, Andrews and Hochstrasser [14]. These workers used two laser CARS to study pentacene doped into benzoic acid crystals at 2 K. Since only two lasers were used in this work, it was not possible to be fully resonant. As shown in figure 1, the laser with frequency Ω_1 was tuned to the pentacene ($o \rightarrow o'$) electronic transition origin and Ω_2 was scanned. Changing Ω_2 simultaneously scans the vibrational and vibronic resonances. The figure also compares the CARS spectrum with fluorescence and absorption spectra of the same sample. There are three vibrational modes at 756, 763 and 787 cm^{-1} in the fluorescence and CARS spectra and three vibronic modes at 747, 761 and 791 cm^{-1} in the absorption and CARS spectra. The authors also reported narrowing of the transitions because of selection within the inhomogeneously broadened band by the Ω_1 laser.

1.2. *Fundamentals*

Nonlinear mixing is the result of nonlinearities in the polarization induced in an electron cloud by an applied electric field [8]. If the functionality of this relationship is

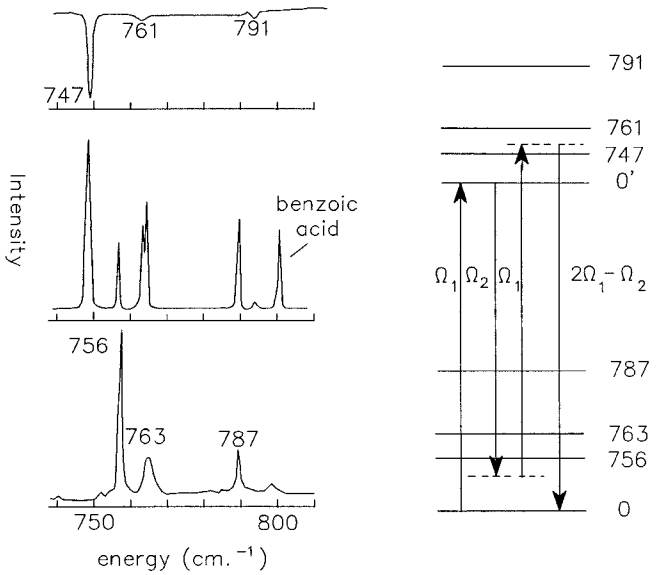

Figure 1. Comparison of pentacene in benzoic acid absorption (top), two-laser CARS (middle), and fluorescence (bottom) spectra at 2 K. The Ω_1 laser was resonant with the electronic transition while the Ω_2 laser was scanned. The numbers show the correspondence between the different spectra [14].

Downloaded At: 17:36 21 January 2011

not known, it can be described phenomenologically by a Taylor series expansion in the electric field,

$$\boldsymbol{P} = \chi^{(1)}\boldsymbol{E} + \chi^{(2)}\boldsymbol{E}^2 + \chi^{(3)}\boldsymbol{E}^3 + \ldots, \tag{1}$$

where $\chi^{(n)}$ is the macroscopic susceptibility.

When a low-intensity laser field propagates through a material, its electric field induces a sinusoidally oscillating polarization ($\chi^{(1)}E$) that launches its own electromagnetic wave at the same frequency as the laser field. Interference between this new field and the applied field leads to absorption, stimulated emission, and linear dispersion of the index of refraction.

If the laser is focused to high intensities, the very large electric fields within the focal volume can become comparable to the electron binding energies and the higher order nonlinearities of equation (1) become important. The induced polarization will be distorted from its sinusoidal shape and it is the Fourier components of the distortion that are responsible for the new frequencies of light that are generated in nonlinear mixing [29].

The Fourier components of the nonlinear polarization include frequencies at all the sum and difference frequencies of the input lasers. The second-order term of equation (1) is responsible for mixing two laser frequencies (Ω_1 and Ω_2) to produce outputs at 0, $2\Omega_1$(or $2\Omega_2$), and $\Omega_1 \pm \Omega_2$, corresponding to the processes of optical rectification, second-harmonic generation, and sum/difference frequency mixing, respectively. The third term is responsible for output frequencies at Ω_1, $2\Omega_i \pm \Omega_j$, $\Omega_1 \pm \Omega_2 \pm \Omega_3$, and $3\Omega_i$, where i, j, k can be any of the input laser frequencies. These output frequencies represent Raman gain and loss, CARS and CSRS, multiresonant four-wave mixing, frequency tripling, as well as saturation of first-order phenomena. There are also higher-order

terms that are responsible for such techniques as hyper-Raman scattering [30], a $\chi^{(5)}$ process.

In an isotropic medium, all of the even terms in this expansion must vanish since the polarization must reverse sign when the electric field reverses [31]. Thus, second-harmonic and sum and difference frequency generation arise only in anisotropic media. For isotropic materials, CARS and the other four-wave mixing (third-order) effects are the lowest order nonlinearities allowed.

Figure 1 shows the energy level diagram associated with CFWM giving an output at frequency $2\Omega_1 - \Omega_2$. The size of the oscillating polarization is enhanced when there is a real molecular state at $\Omega_1, \Omega_1 - \Omega_2$, or $2\Omega_1 - \Omega_2$. Typically the enhancement is a factor of 10^3 per resonance in molcular systems although it can vary greatly for different resonances. CARS is typically performed by monitoring the intensity of the output at $2\Omega_1 - \Omega_2$ while scanning Ω_2. When $\Omega_1 - \Omega_2$ and $2\Omega_1 - \Omega_2$ match vibrational or vibronic resonances, respectively, there is an enhancement in the output efficiency and a Raman-like line is observed. If there is also an electronic resonance with Ω_1, there is a second enhancement that is multiplicative to the first. If there are no resonances with the sample, there will still be a four-wave mixing signal coming from the inherent third-order polarizability of the sample. This signal is responsible for the nonresonant background that dictates the detection limits in CARS and other four-wave mixing methods. The nonresonant polarizability typically arises from high lying electronic states that are far from resonance but which have very large oscillator strengths.

Downloaded At: 17:36 21 January 2011

2. Theory

2.1. *Perturbative approaches*

2.1.1. *Analytic theory*

The four-wave mixing efficiency is controlled by $\chi^{(3)}$ in equation 1. A closed form expression can be obtained for $\chi^{(3)}$ using third-order perturbation theory [32–36].

The wave function $\Psi(\boldsymbol{r}, t)$ changes in time because of an applied net electromagnetic field,

$$E = E_1^0 \exp(\mathrm{i}(\Omega_1 t - k_1 z)) + E_2^0 \exp(\mathrm{i}(\Omega_2 t - k_2 z)) + E_3^0 \exp(\mathrm{i}(\Omega_3 t - k_3 z)) + \text{c.c.}, \quad (2)$$

at frequencies, wavevectors and amplitudes Ω_1, k_i, and E_i^0, respectivedly. The time evolution of $\Psi(\boldsymbol{r}, t)$ is described by the time dependent Schroedinger wave equation,

$$\frac{\partial \Psi(\boldsymbol{r}, t)}{\partial t} = -\frac{\mathrm{i}}{\hbar}(H^0 + V)\Psi(\boldsymbol{r}, t), \quad (3)$$

where $V = -\boldsymbol{\mu} \cdot \boldsymbol{E}$ describes the interaction between the electromagnetic field and the molecule. It can also include the stocastic fields from thermal fluctuations of the matrix that leads to dephasing and relaxion effects. Time-dependent linear combinations of the unperturbed molecular basis states of the unperturbed molecular Hamiltonian, H^0, can describe the time dependent wavefunction,

$$\Psi(\boldsymbol{r}, t) = \sum_n c_n(t)\psi_n(\vec{\boldsymbol{r}}). \quad (4)$$

since they represent a complete and orthonormal basis set.

To understand the temporal evolution of the time-dependent wavefunction, the time dependence of the coefficients, $c_n(t)$, must be determined. Density matrix formalism

is the most powerful way to determine the behaviour of the c_n. A density matrix element is defined by

$$\rho_{\alpha\beta} \equiv c_\alpha c_\beta^*. \tag{5}$$

Populations correspond to the diagonal elements, $\rho_{\alpha\alpha}$, while the off-diagonal elements, $\rho_{\alpha\beta}$, define the size of time dependent coherent states that are linear combinations of states α and β oscillating at a frequency $\omega_\alpha - \omega_\beta$. If one watches such a time-dependent state oscillate between states described by ψ_α and ψ_β, it becomes apparent that they can correspond to states where charge is sloshing back and forth at $\omega_\alpha - \omega_\beta$ and that it is this motion that is responsible for radiated electromagnetic waves at that frequency [37]. Thus, $\rho_{\alpha\beta}$ is proportional to the transition dipole moment of the $\alpha \rightarrow \beta$ transition.

The temporal dependence of the density matrix is defined by the Liouville equation [36],

$$\dot{\rho}_{\alpha\beta} + i\omega_{\alpha\beta}\rho_{\alpha\beta} = \frac{i}{\hbar}[\rho, V]_{\alpha\beta} - \Gamma_{\alpha\beta}\rho_{\alpha\beta} + \delta_{\alpha\beta}\sum_{\varepsilon(\neq\alpha)} \gamma_{\varepsilon\alpha}\rho_{\varepsilon\varepsilon}, \tag{6}$$

where $\omega_{\alpha\beta} = \omega_\alpha - \omega_\beta$ and $\Gamma_{\alpha\beta}$ are the frequency differences and the dephasing rates of the $\alpha \leftrightarrow \beta$ transition. $\gamma_{\varepsilon\alpha}$ are the population relaxation rates between the populations represented by $\rho_{\varepsilon\varepsilon}$ and $\rho_{\alpha\alpha}$.

In the rotating-wave approximation, the lasers induce a polarization that oscillates at the frequencies of the laser or combinations of the frequencies. The amplitude and the optical frequency are conveniently separated by defining

$$\rho_{\alpha\beta} \equiv \rho \exp(-is_{\alpha\beta}\Omega_{\alpha\beta}t), \tag{7}$$

where $s_{\alpha\beta}$ is the sign of $\omega_{\alpha\beta}$ and $\Omega_{\alpha\beta}$ is the laser frequency combination (a positive number) closest to resonance with the $\alpha\beta$ transition. The amplitude of the induced polarization, ρ, will be only slowly varying if the lasers are close to resonance. Each laser frequency induces a Rabi frequency

$$W_{\alpha\beta} \equiv \begin{cases} E^0\mu_{\alpha\beta}/\hbar, & \omega_{\alpha\beta} < 0, \\ (E^0)^*\mu_{\alpha\beta}/\hbar, & \omega_{\alpha\beta} > 0, \end{cases} \tag{8}$$

where E^0 is the amplitude of the resonant laser and $\mu_{\alpha\beta}$ is the dipole moment of the transition. Note that $W_{\alpha\beta}^* = W_{\beta\alpha}$.

Using the rotating-wave approximation, equation (6) for the slowly varying amplitude becomes [36–38]

$$\dot{\rho}_{\mu\nu} = \sum_{\alpha,\beta} (i\Delta_{\mu\nu}\delta_{\mu\alpha}\delta_{\nu\beta} + \delta_{\alpha\beta}\delta_{\mu\nu}\gamma_{\beta\mu} + i\delta_{\nu\beta}W_{\mu\alpha} - i\delta_{\mu\alpha}W_{\beta\nu})\rho_{\alpha\beta}, \tag{9a}$$

where

$$\Delta_{\alpha\beta} \equiv \omega_{\alpha\beta} - s_{\alpha\beta}\Omega_{\alpha\beta} - i\Gamma_{\alpha\beta} \tag{9b}$$

and

$$\gamma_{\alpha\alpha} \equiv 0. \tag{9c}$$

The first term contains the dephasing rate of the $\alpha\beta$ transition while the second term describes population relaxation between states α and β. The last two terms describe transitions induced by the electromagnetic field where either state α (the ket state in $\rho_{\alpha\beta}$) evolves to state μ because of the interaction with the field described by Rabi frequency

Downloaded At: 17:36 21 January 2011

$W_{\mu\alpha}$ or state β (the bra state in $\rho_{\alpha\beta}$) evolves to state v because of the interaction with the field described by Rabi frequency $W_{\beta v}$. Carrying out the summation in equation (9 *a*) gives the simplified expression,

$$\dot{\rho}_{\mu v} = -\mathrm{i}\Delta_{\mu v}\rho_{\mu v} + \sum_{\alpha}[\mathrm{i}(W_{\mu\alpha}\rho_{\alpha v} - W_{\alpha v}\rho_{\mu\alpha}) + \delta_{\mu v}\gamma_{\alpha\mu}\rho_{\alpha\alpha}]. \tag{10}$$

In the perturbative picture, equation (10) may be solved by iteratively substituting the density matrix elements of a given order on the right. Integration then gives the elements of the next higher order. This procedure is generally only practical for low orders. Typically, therefore, only those density matrix elements connected to the initial state by the fewest number of interactions are considered.

For example, in CARS an initial population described by $\rho_{aa}^{(0)}$ interacts with the laser at frequency Ω_{ca} causing an evolution to the coherent state, ρ_{ca}. Assuming ρ_{aa} is the only nonzero initial density matrix element, equation (10) gives

$$\dot{\rho}_{ca} = -\mathrm{i}\Delta_{ca}\rho_{ca} + \mathrm{i}W_{ca}\rho_{aa}^{(0)}, \tag{11}$$

where $\Delta_{ca} = \omega_{ca} - \Omega_{ca} - \mathrm{i}\Gamma_{ca}$ and $W_{ca} = \mu_{ca}(E_{ca}^{0})^{*}/\hbar$. At this level of approximation the only nonzero density matrix elements are ρ_{aa}, ρ_{ca}, and $\rho_{ac} = \rho_{ca}^{*}$. State ρ_{ca} may then evolve to state ρ_{ba} by interaction with the laser at frequency Ω_{cb}. Substituting into (10) gives

$$\dot{\rho}_{ba} = -\mathrm{i}\Delta_{ba}\rho_{ba} + \mathrm{i}W_{bc}\rho_{ca}, \tag{12}$$

where $\Delta_{ba} = \omega_{ba} - \Omega_{ca} + \Omega_{cb} - \mathrm{i}\Gamma_{ba}$ and $W_{bc} = \mu_{bc}E_{cb}^{0}/\hbar$. Finally, state ρ_{ba} evolves to state ρ_{da} by interaction with the third laser,

$$\dot{\rho}_{da} = -\mathrm{i}\Delta_{da}\rho_{da} + \mathrm{i}W_{db}\rho_{ba}, \tag{13}$$

where $\Delta_{da} = \omega_{da} - \Omega_{ca} + \Omega_{cb} - \Omega_{db} - \mathrm{i}\Gamma_{da}$ and $W_{db} = \mu_{db}(E_{db}^{0})^{*}/\hbar$. The amplitude described by ρ_{da} is proportional to the macroscopic dipole that is responsible for the CARS output.

Equations (11)–(13) describe the temporal evolution of the CARS process. In the steady state ($\dot{\rho}_{ca} = \dot{\rho}_{ba} = \dot{\rho}_{da} = 0$) one readily obtains,

$$\rho_{da} = \frac{W_{ac}W_{cb}W_{bd}}{\Delta_{ca}\Delta_{ba}\Delta_{da}}\rho_{aa}^{(0)} = \frac{W_{ac}W_{cb}W_{bd}}{\Delta_{ca}\Delta_{ba}\Delta_{da}}. \tag{14}$$

Since we assumed that a was the only initially populated state, $\rho_{aa}^{(0)} = 1$. Note that this expression is independent of the population feeding terms appearing in equation (10). This independence from the details of population dynamics is quite different from most incoherent spectroscopies and is one of the truly unique advantages of CFWM.

This simple example suggests that the general steady-state solution of equation (10) might be written as

$$\rho_{\mu v} = \sum_{\alpha}\left(\frac{W_{\mu\alpha}\rho_{\alpha v} - W_{\alpha v}\rho_{\mu\alpha}}{\Delta_{\mu v}} + \delta_{\mu v}\frac{\gamma_{\alpha\mu}}{\Gamma_{\mu\mu}}\rho_{\alpha\alpha}\right). \tag{15}$$

Unfortuately, this expression is clearly incorrect since the solution explodes if $\Gamma_{\mu\mu} = 0$ as would be the case for some stable state μ. This inconsistency can be traced to the fact that the set of equations represented by (10) are not independent since for a closed system,

$$\sum_{\alpha}\rho_{\alpha\alpha} = 1. \tag{16}$$

Downloaded At: 17:36 21 January 2011

Thus, one of the $\rho_{\alpha\alpha}$ equations is redundant and should be replaced by equation (16). A clever way in which to retain the simplicity of equation (15) while explicitly including the population conservation constraints is to define

$$\Gamma_{aa} \equiv -\gamma_{\alpha\alpha} \equiv -\gamma_{\beta\beta} \equiv \ldots \tag{17}$$

for some arbitrary level a, usually selected to be the ground (initial) level. The general steady-state solution may then be written,

$$\rho_{\mu\nu} = \delta_{\mu a}\delta_{\nu a} + \sum_{\alpha}\left(\overline{\delta_{\mu a}\delta_{\nu a}}\,\frac{W_{\mu\alpha}\rho_{\alpha\nu} - W_{\alpha\nu}\rho_{\mu\alpha}}{\Delta_{\mu\nu}} + \delta_{\mu\nu}\frac{\gamma_{\alpha\mu}}{\Gamma_{\mu\mu}}\rho_{\alpha\alpha}\right), \tag{18}$$

where $\overline{\delta_{\mu a}\delta_{\nu a}} \equiv 1 - \delta_{\mu a}\delta_{\nu a}$ specifies that both μ and ν cannot simultaneously be equal to a. Substitution of (17) into (18) yields equation (16) as required.

It is often the case that the energy levels resonant with the laser fields are coupled via population relaxation to other levels not resonant with the lasers. The set of resonant levels therefore forms an open system. It has been shown [36] that such a system may be reduced to an equivalent closed system involving only the radiatively pumped levels. That reduced system is still described by equation (18) provided that the various $\Gamma_{\alpha\alpha}$s and $\gamma_{\alpha\beta}$s are suitably redefined. This reduction invalidates equation (17), and in practice the appropriate population relaxation rates must be determined experimentally.

An important limitation of the rotating-wave approximation used here is that it neglects the possibility of more than one laser field being simultaneously resonant with the same transition. For monochromatic lasers and for cases where the laser frequencies are distinct, this approximation is good. For finite bandwidths or lasers of comparable frequencies, however, slowly varying components of the density matrix may exist other than those given by equations (7) and (10). These additional terms are particularly important in so-called degenerate CFWM but are beyond the scope of this review.

Downloaded At: 17:36 21 January 2011

2.1.2 *Diagrammatic techniques*

A very convenient and intuitive method for obtaining the pertubative solution is to use the diagrammatic methods introduced by Yee and Gustafson [39], Taran and coworkers [33, 40], Bordé [35], and Carlson and Wright [36].

Bordé diagrams are summarized in figure 2 for the CFWM methods of interest in this paper. The top row shows the energy level scheme for each CFWM process while the lower part shows the time evolution diagrams. Time (or equivalently, the order of perturbation) begins at the bottom of each diagram and evolves vertically. The two vertical lines represent the simultaneous evolution of the bra (right-hand line) and ket (left-hand line) parts of the wavefunction. Upward slanted lines represent interaction with field components oscillating as $e^{-\Omega t}$ while downward slanted lines correspond to components at $e^{i\Omega t}$. In the rotating-wave approximation only certain interactions are retained as expressed by the delta functions in equation (10). Upward slanted lines on the ket may occur only if the final state is higher than the initial and the opposite is true on the bra. A downward line on the ket only occurs if the final state is lower than the initial, and vice versa on the bra. The states connected by the transition are written as letters on either side of the interaction represented by the intersection of the slanted and vertical lines. The coherent states that are formed during the evolution of the system from the initially populated state are found by reading across the vertical lines to find the bra and ket states that have been formed at any given time or level of perturbation.

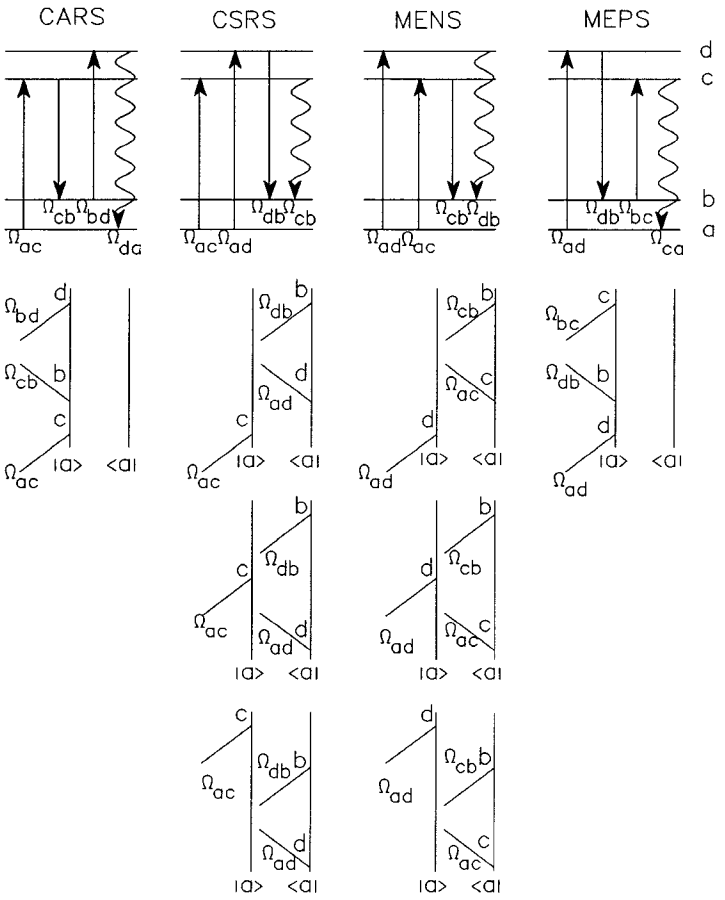

Figure 2. Energy level (*a*) and Bordé (*b*) diagrams for coherent anti-Stokes Raman spectroscopy (CARS), coherent Stokes Raman spectroscopy (CSRS), multiply enhanced nonparametric spectroscopy (MENS), and multiply enhanced parametric spectroscopy (MEPS).

For the CARS diagram on the left of figure 2, the system begins with the population in the ground state represented by ρ_{aa} and evolves through the coherences ρ_{ca}, ρ_{ba} and ρ_{da}. It is important to realize that the evolution to the oscillating dipole at the $d \leftrightarrow a$ transition involves only induced coherences. It does not involved any population changes, suggesting that quenching effects do not enter into a CARS experiment directly. Quenching enters only through its effect on the various linewidths (Γs).

Table 1 summarizes the rotating-wave approximation guidelines for writing the resonance expression for $\rho_{\alpha\beta}$ from the Bordé diagrams [36], including the effects of population conservation discussed in the previous section. Each interaction in a diagram introduces a factor shown on the bottom line of table 1 so the final expression for $\rho_{\alpha\beta}$ is the product of each factor. The corresponding temporal dependence of the oscillating polarization is shown in the second to the last row. The table also contains diagrams that describe feeding effects where a population such as $\rho_{\alpha\alpha}$ relaxes to $\rho_{\gamma\gamma}$. Feeding is indicated by a horizontal dashed line cutting both the ket and bra time evolution.

Note that in table 1, radiative pumping into the initial state a is not allowed. This restriction reflects substitution of the population conservation constraint (equation 16)

Downloaded At: 17:36 21 January 2011

Modified Bordé Digram	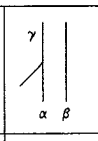	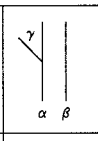	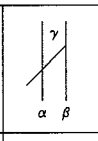	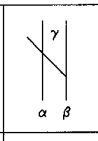	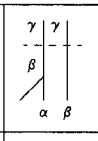	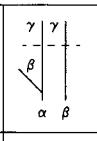	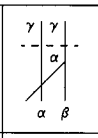	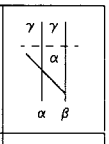
Energy Level Diagram	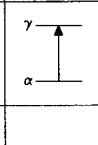	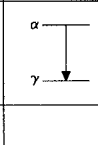	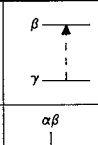	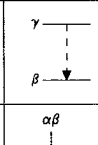	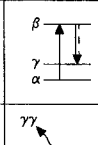	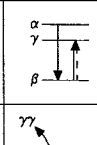	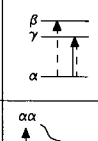	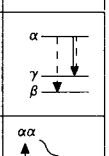
Liouville Diagram Pathway	$\alpha\beta \longrightarrow \gamma\beta$	$\alpha\beta \longrightarrow \gamma\beta$	$\alpha\beta \downarrow \alpha\gamma$	$\alpha\beta \downarrow \alpha\gamma$	$\gamma\gamma \searrow \alpha\beta \longrightarrow \beta\beta$	$\gamma\gamma \searrow \alpha\beta \longrightarrow \beta\beta$	$\alpha\alpha \searrow \alpha\beta \quad \gamma\gamma \uparrow$	$\alpha\alpha \searrow \alpha\beta \quad \gamma\gamma \uparrow$
Consequence of RWA	$\omega_{\alpha\gamma} < 0$	$\omega_{\alpha\gamma} > 0$	$\omega_{\beta\gamma} > 0$	$\omega_{\beta\gamma} < 0$	$\omega_{\alpha\beta} < 0$	$\omega_{\alpha\beta} > 0$	$\omega_{\beta\alpha} > 0$	$\omega_{\beta\alpha} < 0$
Consequence of Population Conservation	$\gamma \neq \beta$	$\gamma \neq \beta$	$\gamma \neq \alpha$	$\gamma \neq \alpha$	$\beta \neq a$	$\beta \neq a$	$\alpha \neq a$	$\alpha \neq a$
Field Component	$E^* e^{-i\Omega_{\alpha\gamma} t}$	$E\, e^{i\Omega_{\alpha\gamma} t}$	$E^* e^{-i\Omega_{\beta\gamma} t}$	$E\, e^{i\Omega_{\beta\gamma} t}$	$E^* e^{-i\Omega_{\alpha\beta} t}$	$E\, e^{i\Omega_{\alpha\beta} t}$	$E^* e^{-i\Omega_{\alpha\beta} t}$	$E\, e^{i\Omega_{\alpha\beta} t}$
Multiplicative Factor	$\frac{W^*_{\alpha\gamma}}{\Delta_{\gamma\beta}}$	$\frac{W^*_{\alpha\gamma}}{\Delta_{\gamma\beta}}$	$\frac{-W_{\beta\gamma}}{\Delta_{\alpha\gamma}}$	$\frac{-W_{\beta\gamma}}{\Delta_{\alpha\gamma}}$	$\mathcal{F}_{\beta\gamma}\frac{W^*_{\alpha\beta}}{\Delta_{\gamma\gamma}}$	$\mathcal{F}_{\beta\gamma}\frac{W^*_{\alpha\beta}}{\Delta_{\gamma\gamma}}$	$-\mathcal{F}_{\alpha\gamma}\frac{W_{\beta\alpha}}{\Delta_{\gamma\gamma}}$	$-\mathcal{F}_{\alpha\gamma}\frac{W_{\beta\alpha}}{\Delta_{\gamma\gamma}}$

Table 1. Guidelines for finding resonance factors for modified Bordé diagrams, energy level diagrams or Liouville diagrams.

Downloaded At: 17:36 21 January 2011

for the rate equation expressed by equation (10) for the evolution of state a. In effect this restriction means that one calculated ρ_{aa} by first calculating all the other $\rho_{\alpha\alpha}$ and then using

$$\rho_{aa} = 1 - \sum_{\alpha \neq a} \rho_{\alpha\alpha}.$$

The quantities $\mathcal{F}_{\alpha\beta}$ are generalized feeding factors representing the population feeding of state β by state α. The explicit form of $\mathcal{F}$ has been given elsewhere [35] in terms of a summation over the appropriate feeding rates. It can be shown that the off-diagonal elements of $\mathcal{F}$ are simply the quantum efficiencies for the associated feeding pathway. The diagonal elements reflect reversible feeding where population from some level is temporarily transferred to a bath of states, but ultimately returned to that same state. In the absence of reversible feeding $\mathcal{F}_{\alpha\alpha} = 1$. For a ground state a, it may also be shown that $\mathcal{F}_{aa}$ is the initial fractional population of level α. Furthermore, for any level $\alpha \neq a$, $\mathcal{F} = -\Gamma_{aa}/\Gamma_{\alpha\alpha}$ in the absence of reversible feeding.

Hochstrasser and coworkers [41, 42] proposed the alternative diagrams shown on the second row of table 1. The arrow direction corresponds to the slant direction of the Bordé diagram. Interactions with the ket are shown with solid arrows while interactions with the bra are shown by dotted arrows. The time ordering of the successive interactions is indicated by the ordering of the arrows from left to right. These diagrams show the relative energies of each state during successive interactions but they do not clearly show the current state of the bra and ket during the time evolution. The alternative convention of Lee and Albrecht associates the arrow direction with the temporal evolution of states [43]. Either of these aproaches provides easily visualized information about the resonances that is equivalent to the Bordé diagrams.

The most powerful diagrammatic method is the Liouville space diagram introduced by Mukamel and coworkers [44, 45] and illustrated in the third row of table 1 within the rotating-wave approximation. The diagrams shows the subscripts of the $\rho_{\alpha\beta}$

as they evolve through successive interactions. Evolution of the bra and ket are distinguished by arranging the interactions in orthogonal directions. Although they do not show the resonances as clearly as the energy level diagrams, they do show all the pathways through which a coherence can evolve. This information is crucial to understanding higher order saturation effects in multiwave mixing methods.

2.2. *Parametric and nonparametric nonlinear mixing methods*

Nonlinear mixing methods can be divided into parameteric and nonparametric processes [22, 46]. There is no energy imparted to the system by a parametric process since the final state is the same as the initial state. CARS is an example of a parametric process. The system starts in a state described by ρ_{aa} and evolves to a coherence described by ρ_{da}. When this coherence launches the output wave, the system returns to ρ_{aa}. In a nonparametric process, there is energy imparted to the system and the final state is different from the initial state. In coherent Stokes Raman scattering (CSRS) for example, the initial state, ρ_{aa}, evolves to the coherence, ρ_{cb}. When a photon is emitted, the system finishes with the population, ρ_{bb}, so energy has been absorbed from the fields.

In terms of the evolution of the density matrix, a parametric process involves altering only the bra or ket of the wavefunction, but not both. A nonparametric process involves evolution of both the bra and ket.

The lowest order Bordé diagram for CARS is shown in figure 2 and involves successive interactions that change only the ket. Figure 3 shows the complete Liouville space diagram for CARS neglecting feeding effects between levels. The shortest or lowest order path between ρ_{aa} and ρ_{da} is third order and is given by the top row in the matrix as $\rho_{aa} \rightarrow \rho_{ca} \rightarrow \rho_{ba} \rightarrow \rho_{da}$. There are an infinite number of higher order pathways that could be taken and these correspond to an exact expression for the mixing within the rotating wave approximation. Note that pathways starting from an excited state population (e.g. ρ_{cc}) would be nonparametric processes if they terminate at ρ_{da}. This fact will have important consequences in the line narrowing capabilities of CARS.

Downloaded At: 17:36 21 January 2011

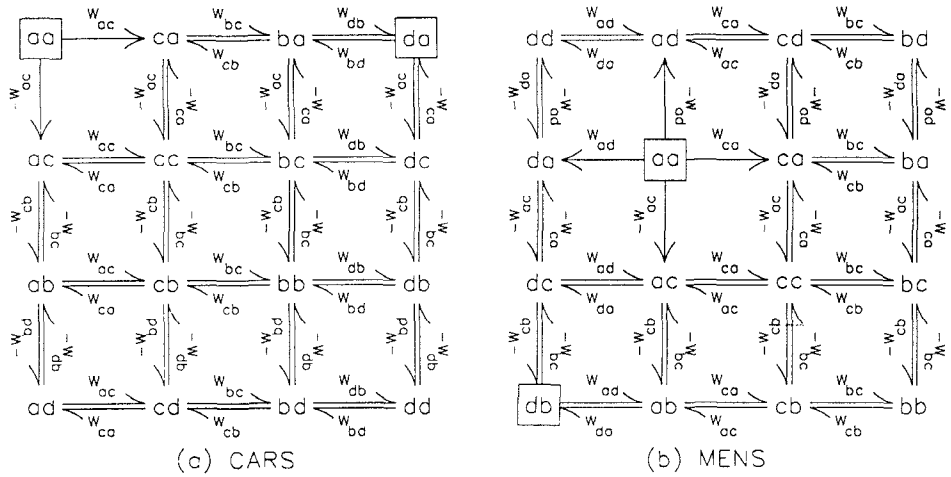

Figure 3. Liouville diagrams for CARS (left) and MENS (right). The initially populated state (*a*) and the final coherent state are shown in boxes. The arrows label field interactions via the Rabi frequencies indicated. Diagram (*a*) also applies to MEPS if *c* and *d* are interchanged. Similarly, exchanging *c* and *d* in (*b*) gives the Liouville diagram for CSRS.

Figure 2 also shows the Bordé diagrams for multiply enhanced nonparametric spectroscopy (MENS) [47]. There are three equivalent processes that can provide a coherence at ρ_{db}. They differ in the time ordering of the interactions with the fields. Figure 3 shows the Liouville diagram for MENS and again one can see there are three equivalent third-order pathways between aa and db: $\rho_{aa}\rightarrow\rho_{ac}\rightarrow\rho_{ab}\rightarrow\rho_{db}$, $\rho_{aa}\rightarrow\rho_{ac}\rightarrow\rho_{dc}\rightarrow\rho_{db}$ and $\rho_{aa}\rightarrow\rho_{da}\rightarrow\rho_{dc}\rightarrow\rho_{db}$. One can also see that mixing processes that begin from an excited population, ρ_{cc}, will be nonparametric if they evolve to the ρ_{db} coherence.

The energy level diagrams in figure 2 use the convention of Albrecht except the bra and ket are not distinguished by solid and dotted lines [43]. In this convention, the direction of the arrows does not correspond to absorption or emission but instead shows the time evolution of the bra and ket involved in the coherence. Diagrams are also shown for coherent Stokes Raman spectroscopy (CSRS) and multiply enhanced parametric spectroscopy (MEPS).

The Bordé diagrams of the Liouville diagram for MENS can be used to derive the expression,

$$\rho_{db}^{(3)}=\left[\frac{W_{da}W_{ac}W_{cb}}{\Delta_{da}\Delta_{dc}\Delta_{db}}+\frac{W_{ac}W_{da}W_{cb}}{\Delta_{ac}\Delta_{dc}\Delta_{db}}+\frac{W_{ac}W_{cb}W_{da}}{\Delta_{ac}\Delta_{ab}\Delta_{db}}\right] \tag{19a}$$

$$=\frac{W_{da}W_{ac}W_{cb}}{\Delta_{db}}\left[\frac{1}{\Delta_{ac}\Delta_{ab}}+\frac{1}{\Delta_{dc}}\left(\frac{1}{\Delta_{da}}+\frac{1}{\Delta_{ac}}\right)\right]. \tag{19b}$$

There are three terms in this expression that correspond to the three pathways that exist in third order and each has a different set of resonances.

The three terms of equation (19) can have different signs and can interfere with each other so the actual resonances observed experimentally can behave quite differently from that expected from the individual terms. One can show that resonance denominators that share a subscript are related by

$$\Delta_{\alpha\eta}+\Delta_{\eta\beta}=\Delta_{\alpha\beta}+\mathrm{i}\Gamma^{\eta}_{\alpha\beta} \tag{20a}$$

where

$$\Gamma^{\eta}_{\alpha\beta}\equiv\Gamma^{*}_{\alpha\beta}-\Gamma^{*}_{\alpha\eta}-\Gamma^{*}_{\eta\beta}-\Gamma_{\eta\eta}=\Gamma_{\alpha\beta}-(\Gamma_{\alpha\eta}+\Gamma_{\eta\beta}) \tag{20b}$$

and $\Gamma^{*}_{\alpha\beta}$ is the pure dephasing rate of the $\alpha\leftrightarrow\beta$ transition [36]. If η is the ground state a, $\Gamma_{aa}=0$ so in the limit where there is no pure dephasing, $\Gamma^{a}_{\alpha\beta}=0$ and $\Delta_{\alpha a}+\Delta_{a\beta}=\Delta_{\alpha\beta}$.

Equation (20) can be used to rewrite equation (19) in the form [48],

$$\rho_{db}^{(3)}=\frac{W_{da}W_{ac}W_{cb}}{\Delta_{ac}\Delta_{da}}\left[\frac{1}{\Delta_{ab}}+\frac{\mathrm{i}}{\Delta_{db}}\left(\frac{\Gamma^{a}_{bd}}{\Delta_{ab}}+\frac{\Gamma^{a}_{dc}}{\Delta_{dc}}\right)\right]. \tag{21}$$

In the limit of no pure dephasing, only the first term survives and the observed resonances are Δ_{ac}, Δ_{da}, and Δ_{ab}. When pure dephasing becomes important, the new resonances Δ_{db} and Δ_{dc} appear. These new resonances are known as pressure-induced extra resonances in 4 wave mixing (PIER4) [49] or dephasing-induced coherent emission (DICE) [17].

2.3. *Nonperturbative treatments*

Multiresonant conditions make saturation effects almost unavoidable in laser driven nonlinear experiments. The perturbative treatments ignore important and potentially useful effects such as line-narrowing that often require higher order or

Downloaded At: 17:36 21 January 2011

nonperturbative treatments. We will consider the higher order solutions for CARS in some depth because the character of the resonances changes when saturation effects become important. These changes will have important consequences on the line narrowing capabilities of CARS.

Equation (18) or the Liouville diagram for CARS (figure 3) in conjunction with table 1 can be used to write the following set of equations that describe all of the induced coherences associated with CARS [22, 38, 50, 51].

$$\Delta_{ca}\rho_{ca} = W_{ca}(\rho_{cc} - \rho_{aa}) + W_{cb}\rho_{ba}, \tag{22 a}$$

$$\Delta_{ba}\rho_{ba} = -W_{ca}\rho_{bc} + W_{bc}\rho_{ca} + W_{bd}\rho_{da}, \tag{22 b}$$

$$\Delta_{dc}\rho_{dc} = -W_{ac}\rho_{da} - W_{bc}\rho_{db} + W_{db}\rho_{bc}, \tag{22 c}$$

$$\Delta_{db}\rho_{db} = -W_{cb}\rho_{dc} - W_{db}(\rho_{dd} - \rho_{bb}), \tag{22 d}$$

$$\Delta_{cb}\rho_{cb} = W_{ca}\rho_{ab} - W_{cb}(\rho_{cc} - \rho_{bb}) - W_{db}\rho_{cd}, \tag{22 e}$$

$$\Delta_{da}\rho_{da} = -W_{ca}\rho_{dc} + W_{db}\rho_{ba}. \tag{22 f}$$

These equations can be solved simultaneously to yield the expression [22, 53],

$$\rho_{da} = \frac{W_{ca}W_{cb}W_{db}}{\Delta}\{A(\rho_{cc} - \rho_{aa}) + B(\rho_{cc} - \rho_{bb}) + C(\rho_{dd} - \rho_{bb})\}, \tag{23 a}$$

where

$$\Delta = \Delta_{da}\alpha\beta - |W_{ac}|^2\Delta_{db}\Delta_{cb}^*(\alpha - |W_{bd}|^2\Delta_{ca}\beta) - |W_{bd}|^2\Delta_{ca}\Delta_{cb}^*\beta^2 - |W_{ac}|^4|W_{bd}|^2\Delta_{ca}\Delta_{cb}^*\Delta_{db}^2, \tag{23 b}$$

$$A = -\Delta_{cb}^*\beta^2 + |W_{ac}|^2\Delta_{cb}^*\Delta_{db}\beta, \tag{23 c}$$

$$B = \alpha\Delta_{db} - |W_{ac}|^2\Delta_{ca}\Delta_{db}\beta + |W_{ac}|^2|W_{bd}|^2\Delta_{ca}\Delta_{db}^2 + \Delta_{ca}\beta^2 - |W_{bd}|^2\Delta_{ca}\Delta_{db}\beta, \tag{23 d}$$

$$C = -\alpha\Delta_{cb}^* - |W_{ac}|^2|W_{bd}|^2\Delta_{ca}\Delta_{cb}^*\Delta_{db} + |W_{bd}|^2\Delta_{ca}\Delta_{cb}^*\beta, \tag{23 e}$$

$$\alpha = \beta\gamma - |W_{ac}|^2|W_{bd}|^2\Delta_{ca}\Delta_{db}, \tag{23 f}$$

$$\beta = \Delta_{cb}^*\Delta_{dc}\Delta_{db} - \Delta_{cb}^*|W_{cb}|^2 + \Delta_{db}|W_{bd}|^2, \tag{23 g}$$

and

$$\gamma = \Delta_{ca}\Delta_{ba}\Delta_{cb}^* - \Delta_{cb}^*|W_{cb}|^2 + \Delta_{ca}|W_{ac}|^2. \tag{23 h}$$

Note that $\Delta_{\alpha\beta}^* = -\Delta_{\beta\alpha}$.

The primary difficulty in applying equation (23) is in determining the diagonal density matrix elements which depend strongly on the feeding rates and pathways for the system under consideration. Fortunately, it is rarely necessary to use the full expression for ρ_{da} and several approximations are possible.

If one considers only contributions up to fifth order and assumes only levels a and c to be appreciably populated, equation (23) becomes

$$\rho_{da} = W_{ca}W_{bc}W_{db}\left[\left[\frac{\rho_{aa}^{(0)} + \rho_{aa}^{(2)}}{\Delta_{ca}\Delta_{ba}\Delta_{da}} + \rho_{aa}^{(0)}\left\{\frac{|W_{ac}|^2}{\Delta_{ca}\Delta_{ba}\Delta_{da}}\left[\frac{1}{\Delta_{da}\Delta_{dc}} + \frac{1}{\Delta_{bc}}\left(\frac{1}{\Delta_{ba}} + \frac{1}{\Delta_{dc}}\right)\right] + \frac{|W_{cb}|^2}{\Delta_{ca}^2\Delta_{ba}^2\Delta_{da}} + \frac{|W_{bd}|^2}{\Delta_{ca}\Delta_{ba}^2\Delta_{da}^2}\right\} - \rho_{cc}^{(2)}\frac{1}{\Delta_{da}}\left[\frac{1}{\Delta_{bc}\Delta_{dc}} + \frac{1}{\Delta_{ba}}\left(\frac{1}{\Delta_{ca}} + \frac{1}{\Delta_{bc}}\right)\right]\right]\right], \tag{24 a}$$

Downloaded At: 17:36 21 January 2011

where

$$\rho_{cc}^{(2)} = \mathscr{F}_{cc} \frac{2\Gamma_{ac}}{\Gamma_{cc}} \left| \frac{W_{ac}}{\Delta_{ac}} \right|^2 \rho_{aa}^{(0)} \tag{24 b}$$

and

$$\rho_{aa}^{(2)} = \mathscr{F}_{ca} \frac{2\Gamma_{ac}}{\Gamma_{aa}} \left| \frac{W_{ac}}{\Delta_{ac}} \right|^2 \rho_{aa}^{(0)}. \tag{24 c}$$

In the absence of feeding, $\mathscr{F}_{cc} = 1$ and $\mathscr{F}_{ca} = -\Gamma_{aa}/\Gamma_{cc}$. Equation (24) can be readily derived by tracing through the various third-order and fifth-order pathways of figure 3 (*a*).

Each of the terms in equation (24 *a*) correspond to different pathways from ρ_{aa} to ρ_{da} and there are again interferences that must be considered between equivalent paths. The expression can be rewritten in the form

$$\rho_{da} = W_{ca} W_{bc} W_{db} \left\{ \left(1 - \rho_{aa}^{(2)} + \frac{|W_{bc}|^2}{\Delta_{ba}\Delta_{ca}} + \frac{|W_{db}|^2}{\Delta_{ba}\Delta_{da}} \right) \frac{1}{\Delta_{ca}\Delta_{ba}\Delta_{da}} \right.$$
$$\left. - \left| \frac{W_{ca}}{\Delta_{ca}} \right|^2 \left[\left(\frac{1}{\Delta_{ca}} + \frac{1}{\Delta_{ba}} + \frac{1}{\Delta_{da}} \right) \frac{1}{\Delta_{da}\Delta_{ba}} + D \right] \right\}. \tag{25 a}$$

where

$$D \equiv \frac{\mathrm{i}}{\Delta_{da}\Delta_{ba}} \left[\frac{\Gamma_{bc}^a}{\Delta_{bc}} \left(\frac{1}{\Delta_{ba}} + \frac{1}{\Delta_{dc}} \right) + \frac{\Gamma_{dc}^a}{\Delta_{da}\Delta_{dc}} \right]$$
$$+ \left(\mathscr{F}_{cc} \frac{2\Gamma_{ac}}{\Gamma_{cc}} - 1 \right) \frac{1}{\Delta_{ca}\Delta_{bc}} \left[\frac{1}{\Delta_{dc}} + \frac{\mathrm{i}}{\Delta_{da}} \left(\frac{\Gamma_{ba}^c}{\Delta_{ba}} + \frac{\Gamma_{da}^c}{\Delta_{bc}} \right) \right], \tag{25 b}$$

and we have assumed $\rho_{aa}^{(0)} = 1$. If there is no pure dephasing ($\Gamma_{bc}^a = \Gamma_{dc}^a = \Gamma_{ba}^c = \Gamma_{da}^c = 0$) nor reversible feeding for level c ($\mathscr{F}_{cc} = 1$), then $D = 0$. Each of the surviving terms has a different character that will become important when the line narrowing capabilities of different nonlinear mixing methods are considered.

The other important limit for equation (23) is high power for the laser resonant with the $a \leftrightarrow c$ transition but low powers for the other lasers. In this limit and again neglecting population of all levels except a and c [38, 54, 55]

$$\rho_{ad} = W_{ac} W_{cb} W_{bd} \frac{\Delta_{ca}\Delta_{cb}\Delta_{cd} + |W_{ac}|^2(\Delta_{cb} + \Delta_{cd} + \mathrm{i}\Gamma_{cb}^a - f\Delta_{ca})/(1-f)}{|\nabla_{ac}|^2(\Delta_{ad}\Delta_{cd} - |W_{ac}|^2)(\Delta_{ab}\Delta_{cb} - |W_{ac}|^2)}, \tag{26 a}$$

where

$$\nabla_{ac} \equiv \Delta_{ac} + \mathrm{i}\Gamma_{ac}[1 - (1+S)^{1/2}], \tag{26 b}$$

$$a \equiv \Gamma_{ac} \left(\frac{\mathscr{F}_{cc}}{\Gamma_{cc}} - \frac{\mathscr{F}_{ca}}{\Gamma_{aa}} \right), \tag{26 c}$$

$$f \equiv 1 - \left(\frac{2\Gamma_{ac}}{\Gamma_{cc}} \mathscr{F}_{cc}^a \right)^{-1}, \tag{26 d}$$

and

$$S \equiv \frac{2a|W_{ac}|^2}{\Gamma_{ac}^2}. \tag{26 e}$$

Downloaded At: 17:36 21 January 2011

is a measure of the degree of saturation for the ac transition. Two parameters (a and f) account for population feeding. $\mathscr{F}^a_{cc}$ is similar to $\mathscr{F}_{cc}$ except it neglects feeding pathways that involve state a. In the absence of feeding, $a=2\Gamma_{ac}/\Gamma_{cc}$ and $\mathscr{F}^a_{cc}=1$. If both feeding and pure dephasing can be neglected, then $f=0$ and $a=1$.

If W_{ac} is much smaller than the dephasing rate of the vibronic (d) or vibrational (b) resonances, this equation reduces to the simple form [54]

$$\rho_{ad}=\frac{W_{ac}W_{cb}W_{bd}\Delta_{ca}}{\Delta_{ab}\Delta_{ad}|\nabla_{ca}|^2}, \tag{27}$$

and the dominant effect of saturation is to simply broaden the ca transition.

2.4. *Mixing efficiency and absorption effects*

The off-diagonal density matrix elements are proportional to the oscillating polarization that launches the output electromagnetic wave. Neglecting local field effects, the macroscopic CARS polarization (dipole moment per volume) is

$$P(\Omega_4=\Omega_1-\Omega_2+\Omega_3)=N(\rho_{\alpha\beta}\mu_{\beta\alpha}+\rho_{\beta\alpha}\mu_{\alpha\beta}), \tag{28}$$

where N is the number concentration and $\rho_{\alpha\beta}$ and $\rho_{\beta\alpha}$ contain both the amplitude and frequency factors [36]. The intensity of the CARS output that is induced by this polarization is (in cgs units) [54],

$$I_{\mathrm{CARS}}=\frac{2\pi\Omega_4^2N^2F|\rho_{da}|^2\mu_{da}^2}{c}\frac{l^2\sin^2(\Delta kl/2)}{(\Delta kl/2)^2} \tag{29}$$

where $\Delta k=k_1+k_2+k_3-k_4$, Ω_4 is the output frequency, l is the pathlength within the sample, F is a correction factor for local field effects, and c is the speed of light. We have assumed here that the various refractive indices are unity.

An important experimental complication occurs because many mixing experiments must be performed in absorbing samples and the mixing efficiency will be changed by the attenuation of the excitation lasers and the output signal [56]. If the absorption coefficients (defined as α such that $I\propto e^{-\alpha l}$) are α_1, α_2, and α_3 at the three input laser frequencies, $\alpha_S\equiv\alpha_1+\alpha_2+\alpha_3$, and α is the absorption coefficient at the output frequency, the absorption effects can be incorporated into equation (29) by replacing the $\mathrm{sinc}^2(\Delta kl/2)$ function by a function $M(\alpha,\alpha_S,\Delta kl)$ where

$$M=\exp(-\alpha l)\frac{[1-\exp[(\alpha-\alpha_S)l/2)^2+4\exp[(\alpha-\alpha_S)l/2]\sin^2(\Delta kl/2)}{[(\alpha-\alpha_S)l/2]^2+[\Delta kl]^2} \tag{30}$$

If the mixing is phase matched ($\Delta k=0$), this expression reduces to the simple form

$$M=\left[\frac{\exp(-\alpha l/2)-\exp(-\alpha_S l/2)}{(\alpha-\alpha_S)l/2}\right]^2. \tag{31}$$

A detailed discussion of the behaviour of M is given elsewhere [56]. It is important in describing reabsorption dips and changes in the lineshape of peaks in nonlinear mixing experiments where the scanning laser or output signal crosses an absorptive resonance. Equations (30) and (31) are especially convenient because they only depend on the experimentally measurable bulk absorbance $A=\alpha l/\ln(10)$.

At the same time that the output is attenuated by absorption, there can also be an enhancement of the nonlinear susceptibility if the absorptive transition simultaneously

Downloaded At: 17:36 21 January 2011

appears in ρ_{da}. The net effect of the absorption can be determined by relating the absorption coefficient to the mixing efficiency.

In CARS, the absorption is dominated by the *da* and *ca* resonances since a nonzero population difference is expected only for those transitions. The peak absorption cross-section for any transition $\alpha\beta$ is

$$\sigma^0_{\alpha\beta} \equiv \frac{\alpha}{N} = \frac{4\pi\omega_{\alpha\beta}|\mu_{\alpha\beta}|^2}{\hbar c n \Gamma_{\alpha\beta}}. \tag{32}$$

Using the third-order expression for CARS (equation 14) one can express the overall CARS efficiency in terms of the sample absorbances [56].

$$\frac{\mathcal{N}_{da}}{\mathcal{N}_{ca}} = \frac{1}{4} MF \frac{A_{ca}A_{da}}{[\ln(10)]^2}\left[\frac{\mathcal{N}_{bc}\sigma^0_{cb}}{2\Gamma_{cb}}\right]\left[\frac{\mathcal{N}_{bd}\sigma^0_{db}}{2\Gamma_{db}}\right]\left|\frac{\Gamma_{ba}}{\Delta_{ba}}\right|^2 \frac{\Gamma^2_{cb}\Gamma^2_{db}}{\Gamma_{ca}\Gamma_{da}\Gamma^2_{ba}}, \tag{33}$$

where $\mathcal{N}_{\alpha\beta}$ is the photon flux (photons s^{-1} cm^{-2}) resonant with the $a \leftrightarrow \beta$ transition and $A_{\alpha\beta}$ is its wavelength dependent absorbance. This equation relates the CARS mixing efficiency to the absorbances at the electronic (*ac*) and vibronic (*da*) transition frequencies, the relative amount of saturation of the $c \leftrightarrow b$ and $b \leftrightarrow d$ transitions, the relative detuning of the vibrational (*ba*) resonance, and a ratio of linewidths. This expression is only applicable when saturation effects are not large since it is based on the third order perturbative result.

Equation (33) in conjunction with equation (29) predicts an optimum absorbance where the effects of beam attenuation and four-wave mixing enhancement are balanced and the maximum signal is generated [56]. Figure 4 is a contour plot of the CARS intensity as a function of the absorbances at the electronic and vibronic resonance frequencies. A maximum intensity is predicted for absorbances of 0·87 at Ω_{ca} and Ω_{da}.

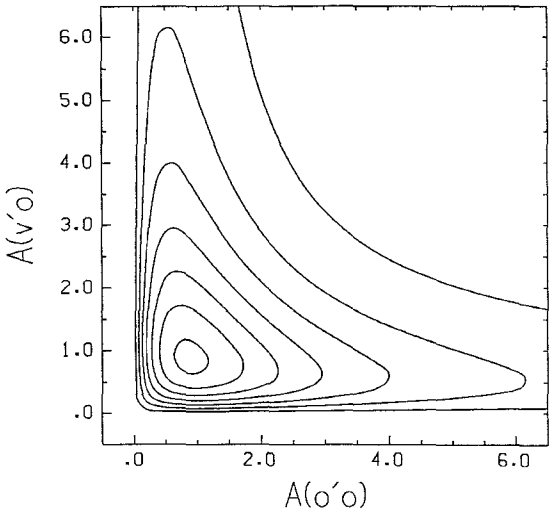

Figure 4. Contour plot of CARS intensity as a function of the absorbances at the o↔o′ and o↔v′ transitions. The peak value is 13·5% of that expected if there was no absorptive attenuation while the contour line closest to the axes is 1%. The interval between contour lines is 2%.

Downloaded At: 17:36 21 January 2011

2.5. *Coherent interference effects and component selection*

The net polarization is the sum of the contributions from all the polarizable components in a material but the observed intensity depends on the square of the polarization. Thus, there will be cross-terms in the intensity expression between different sources that will produce important interference effects, especially in terms of lineshapes.

There are three important interference effects of this variety for multiresonant molecular CFWM: (1) interference between different sites or sample components, (2) interference between two different resonances that arise because the different lasers in a multiwave mixing scheme can be resonant with different transitions simultaneously, and (3) interference between the nonresonant background and the resonant signals. All of these interference effects can be qualitatively described by the following expression for the square of the net third-order susceptibility:

$$|\chi^{(3)}_{\text{net}}|^2 = |\chi^{(3)}_{\text{R1}}(\text{site 1}) + \chi^{(3)}_{\text{R2}}(\text{site 1}) + \chi^{(3)}_{\text{R}}(\text{site 2}) + \chi^{(3)}_{\text{NR}}|^2. \tag{34}$$

The subscripts indicate two resonance pathways exist for site 1 while site 2 has a single resonance pathway. The cross-terms between the first and third terms represents interference between sites. The cross-terms between the first and second terms represent the interference between different resonances of a single site. The cross-terms between the last term and the others represents the interference with the nonresonant background.

The nonresonant background interference with the resonant signal and the interference between two different resonances on a single site have been discussed by others in detail [57, 58]. The nonresonant background causes changes in lineshape when the signal levels become comparable to the nonresonant background. At very low concentrations, doubly resonant features acquire a dispersive shape while single or triply resonant features tend to experience a symmetrical enhancement or attenuation [56]. If there are two resonances near each other, there is an additional interference that can be constructive or destructive depending on the relative signs of the real and imaginary parts of $\chi^{(3)}$ for each resonance.

The interference between different sites is important for understanding the line narrowing capabilities of multiresonant CFWM. For a two-site system, one can write the third-order susceptibility [59] as

$$\chi^{(3)} = \frac{\xi(A + iB)}{|\Delta_{ca}|^2|\Delta_{ba}|^2|\Delta_{da}|^2} + \frac{\xi'(A' + iB')}{|\Delta'_{ca}|^2|\Delta'_{ba}|^2|\Delta'_{da}|^2}, \tag{35a}$$

where

$$A \equiv \delta_{ca}\delta_{ba}\delta_{da} - \delta_{da}\Gamma_{ca}\Gamma_{ba} - \delta_{ca}\Gamma_{ba}\Gamma_{da} - \delta_{ba}\Gamma_{ca}\Gamma_{da}, \tag{35b}$$

$$B \equiv \delta_{ca}\delta_{ba}\Gamma_{da} + \delta_{ca}\delta_{da}\Gamma_{ba} + \delta_{ba}\delta_{da}\Gamma_{ca} - \Gamma_{ca}\Gamma_{ba}\Gamma_{da}, \tag{35c}$$

$$A' \equiv \delta'_{ca}\delta'_{ba}\delta'_{da} - \delta'_{da}\Gamma'_{ca}\Gamma'_{ba} - \delta'_{ca}\Gamma'_{ba}\Gamma'_{da} - \delta'_{ba}\Gamma'_{ca}\Gamma'_{da}, \tag{35d}$$

$$B' \equiv \delta'_{ca}\delta'_{ba}\Gamma'_{da} + \delta'_{ca}\delta'_{da}\Gamma'_{ba} + \delta'_{ba}\delta'_{da}\Gamma'_{ca} - \Gamma'_{ca}\Gamma'_{ba}\Gamma'_{da}, \tag{35e}$$

and

$$\delta_{\alpha\beta} \equiv \omega_{\alpha\beta} - \Omega_{\alpha\beta}. \tag{35f}$$

Downloaded At: 17:36 21 January 2011

ξ is the constant proportional to the density of sites, and the prime quantities indicate the second site. Taking the square,

$$|\chi^{(3)}|^2 = \frac{\xi}{A^2+B^2} + \frac{\xi'}{A'^2+B'^2} + \frac{2(AA'+BB')\xi\xi'}{(A^2+B^2)(A'^2+B'^2)}. \tag{36}$$

The first two terms represent resonances on the separate sites while the last term represents the interference effects between the two sites.

A case of particular interest occurs when one site is triply resonant. This situation arises if an experiment seeks to emphasize the spectra of one component in a mixture by tuning to resonances of that component. If the unprimed site is triply resonant, then $\delta_{\alpha\beta}=0$, $A=0$ and $B=-\Gamma_{ca}\Gamma_{ba}\Gamma_{da}$. The sign of the cross-term therefore depends on the product BB'. If all of the detuning factors, $\delta'_{\alpha\beta}$, of the nonselected site are of the same sign, B' will be positive (assuming the detuning factors are larger than the linewidths) and the cross-term will be negative. The contribution from the second site at the wavelength of complete resonance with the selected site will be destructive. If one of the detuning factors has the opposite sign from the others, B' can be negative depending on the relative size of the detunings and the cross-term would be positive. In this case, the contribution from the second site at the wavelength of complete resonance with the selected site would be constructive.

These arguments are changed if the mixing is a nonparametric process [48]. Using equation (21) for MENS in the no pure dephasing limit as an example,

$$\chi^{(3)}_{\mathrm{MENS}} = \frac{\xi(A+\mathrm{i}B)}{|\Delta_{ac}|^2|\Delta_{ab}|^2|\Delta_{da}|^2} + \frac{\xi'(A'+\mathrm{i}B')}{|\Delta'_{ac}|^2|\Delta'_{ab}|^2|\Delta'_{da}|^2}, \tag{37 a}$$

where now

$$A \equiv \delta_{ca}\delta_{ba}\delta_{da} - \delta_{da}\Gamma_{ca}\Gamma_{ba} + \delta_{ca}\Gamma_{ba}\Gamma_{da} + \delta_{ba}\Gamma_{ca}\Gamma_{da}, \tag{37 b}$$

$$B \equiv -\delta_{ca}\delta_{ba}\Gamma_{da} + \delta_{ca}\delta_{da}\Gamma_{ba} + \delta_{ba}\delta_{da}\Gamma_{ca} + \Gamma_{ca}\Gamma_{ba}\Gamma_{da}, \tag{37 c}$$

$$A' \equiv \delta'_{ca}\delta'_{ba}\delta'_{da} - \delta'_{da}\Gamma'_{ca}\Gamma'_{ba} + \delta'_{ca}\Gamma'_{ba}\Gamma'_{da} + \delta'_{ba}\Gamma'_{ca}\Gamma'_{da}, \tag{37 d}$$

and

$$B' \equiv -\delta'_{ca}\delta'_{ba}\Gamma'_{da} + \delta'_{ca}\delta'_{da}\Gamma'_{ba} + \delta'_{ba}\delta'_{da}\Gamma'_{ca} + \Gamma'_{ca}\Gamma'_{ba}\Gamma'_{da}, \tag{37 e}$$

The absolute square of equation (37 *a*) has the same form as equation (36), but with A, B, A', and B' redefined as above. For this nonparametric case, the fully resonant site will have $A=0$ and $B=\Gamma_{ca}\Gamma_{ba}\Gamma_{ca}$. The sign of the cross-term depends again on the product BB'. If $(\delta_{da}\delta_{ca}\Gamma_{ba}+\delta_{da}\delta_{ba}\Gamma_{ca})>\delta_{ba}\delta_{ca}\Gamma_{da}$, then B' is positive and the cross-term will also be positive. The intersite interference will be constructive at the position of complete resonance with the selected site.

The differences between the intersite interference in a parametric and nonparametric mixing method are illustrated in figure 5 [48]. This figure shows $|\chi^{(3)}|^2$ as the solid line, the contributions from individual sites as the dotted lines, and the cross-term contributions as the broken lines. The destructive and constructive character to the CARS and MENS lineshapes is clear.

2.6. *Line narrowing with multiresonant nonlinear mixing*

The arguments in the previous section can be extended to inhomogeneously broadened systems where there is a continuum of sites. One must now calculate the individual contributions to $\chi^{(3)}$ from single sites and integrate over the inhomogeneous

Downloaded At: 17:36 21 January 2011

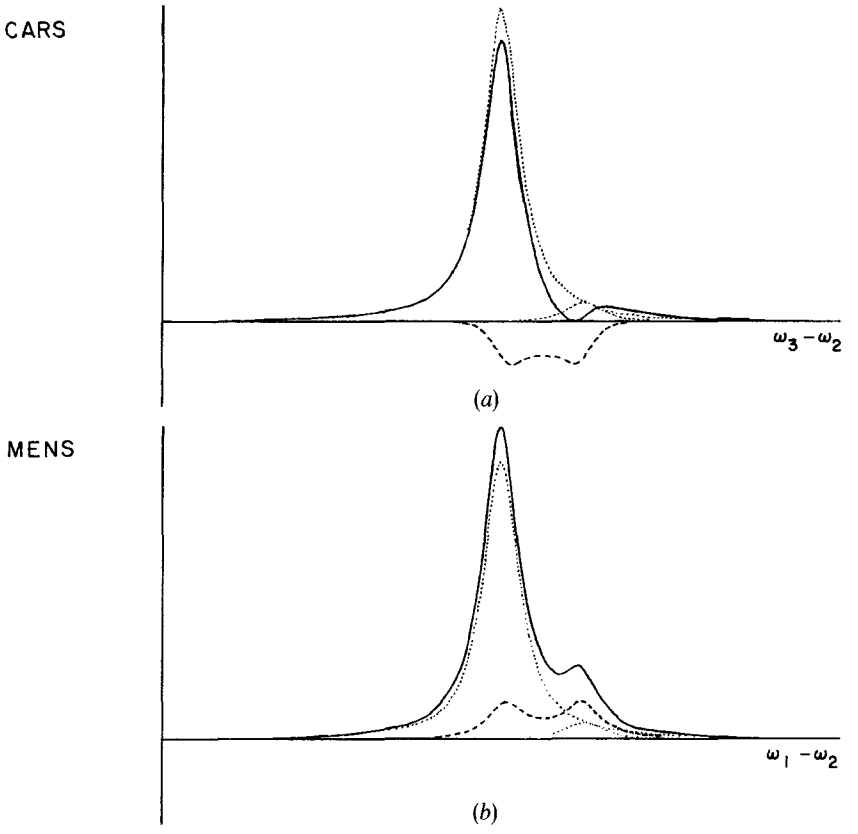

Figure 5. Simulations of CARS and MENS vibronic spectra for a two-component system where the electronically resonant laser has been tuned for one site and the vibronic resonance is scanned. The dotted lines show the individual sites contributions and the dashed lines show the cross-terms between sites.

Downloaded At: 17:36 21 January 2011

distribution. In order to obtain a closed form expression for the integrated mixing efficiency, it has become common to assume that the inhomogeneous broadening can be described by a Lorentzian profile so that contour integration can be used [22, 55, 60–62, 63]. In this approach, the energy levels are shifted in energy by an amount ξ because of the broadening perturbation. The perturbation can be a Doppler shift for gas phase species or a disorder broadening for a condensed phase species [33, 34]. The standard deviation for the shifts is taken to be σ. We shall assume for simplicity that the shifts are correlated and are identical for all levels within one electronic manifold as is typical of molecular systems. Thus the o→o′ transition will be shifted by the same amount as the o→v′ transition and there will be no broadening for the o→v transition.

For CARS, the integration of $\rho_{da}^{(3)}$ over a Lorentzian distribution can be written as

$$\rho_{da}=\frac{\sigma}{\pi}\int_{-\infty}^{\infty}\frac{1}{\xi^2+\sigma^2}\frac{W_{ca}W_{cb}W_{db}}{\Delta_{ca}(\xi)\Delta_{ba}\Delta_{da}(\xi)}\,\mathrm{d}\xi, \tag{38 a}$$

where

$$\Delta_{\alpha\beta}(\xi)\equiv\omega_{\alpha\beta}^0+\xi-s_{\alpha\beta}\Omega_{\alpha\beta}-\mathrm{i}\Gamma_{\alpha\beta} \tag{38 b}$$

and $\omega^0_{\alpha\beta}$ is the centre frequency of the inhomogeneously broadened line at $\alpha \leftrightarrow \beta$. Similarly, for MENS in the no pure dephasing limit,

$$\rho_{db} = \frac{\sigma}{\pi} \int_{-\infty}^{\infty} \frac{1}{\xi^2 + \sigma^2} \frac{W_{ac} W_{cb} W_{da}}{\Delta_{ca}(\xi) \Delta_{ab} \Delta_{ad}(\xi)} \, d\xi. \tag{39}$$

Integrating the two expressions, one obtains

$$\rho^{(3)}_{da}(\text{CARS}) = \frac{W_{ca} W_{cb} W_{da}}{\Delta^-_{ca} \Delta_{ba} \Delta^-_{da}} \tag{40}$$

and

$$\rho^{(3)}_{db}(\text{MENS}) = \frac{W_{cb} W_{ac} W_{da}}{\Delta_{ab} \Delta^+_{da}} \left(\frac{2i\sigma}{\Delta^-_{da}(\Delta_{ac} + \Delta_{da})} + \frac{1}{\Delta^-_{ac}} \right) \tag{41}$$

where

$$\Delta^{\pm}_{\alpha\beta} \equiv \omega^0_{\alpha\beta} - s_{\alpha\beta} \Omega_{\alpha\beta} - i\Gamma_{\alpha\beta} \pm i\sigma = \Delta_{\alpha\beta} \pm i\sigma. \tag{42}$$

The electronic (ca) and vibronic (da) resonances in the CARS expression have the full inhomogeneous width, σ. The first term of the MENS expression shows a new resonance of the form $\Delta_{ac} + \Delta_{da} = \Delta_{dc} + i\Gamma^a_{cd}$. The width of this resonance is determined by the sum of the electronic and vibronic widths and is independent of the inhomogeneous width. Its position is determined by where the real part of $\Delta_{ac} + \Delta_{da}$ becomes zero, namely when $\Omega_{da} - \Omega_{ca} = \omega_{dc}$. This resonance corresponds to those sites selected by Ω_{ca} and which are resonant with Ω_{da}. If either Ω_{ac} or Ω_{da} is changed, the position of the narrow resonance shifts in correspondence. The intensity of the sharp peak scales as $\sigma/(\Delta^+_{da}\Delta^-_{da})$ which defines the full inhomogeneous line profile. The second term in the MENS expression has only inhomogeneously broadened resonances. Overall, therefore, the MENS spectrum should consist of a sharp line-narrowed peak that shifts as a function of either Δ_{ac} or Δ_{da} and is superimposed upon a weak, inhomogeneously broadened background.

It was first pointed out by Oullette and Denariez-Roberge [51] that CARS can develop line-narrowing capabilities when saturation effects become important. The fifth-order expression for CARS given by equation (25 *a*) provides an instructive first approximation to the effects of higher-order terms. Neglecting pure dephasing and feeding ($D = 0$), integration of (25 *a*) over the fifth-order terms gives [52, 63]

$$\frac{\rho^{(5)}_{da}(\text{CARS})}{W_{ca} W_{cb} W_{db}} = -\frac{|W_{ac}|^2}{\Delta^-_{ac} \Delta^+_{ca}} \frac{1}{\Delta^-_{ad} \Delta_{ab}} \left(\frac{2}{\Delta^-_{ac}} + \frac{1}{\Delta_{ab}} + \frac{1}{\Delta^-_{ad}} \right) + \frac{\sigma}{\Gamma_{ac}} \frac{|W_{ac}|^2}{\Delta^+_{ca} \Delta^-_{ca}} \frac{1}{\Delta_{cd} \Delta_{ab}} \left(\frac{i}{\Delta_{ac}} + \frac{1}{\Delta_{ab}} + \frac{1}{\Delta_{cd}} \right). \tag{43}$$

The first set of terms are inhomogeneously broadened but the second displays the line-narrowed vibronic (Δ_{dc}) resonance having the homogeneous width Γ_{dc}. Note that a corresponding line-narrowed vibrational resonance is not predicted. This absence is a direct result of interference between fully coherent terms of $\rho^{(5)}_{da}$ and those which pass through an induced excited state (c) population. That interference effectively cancels the line-narrowed cb resonance otherwise expected from an excited state population.

The complete expression for CARS in fifth-order including feeding and pure dephasing can be found elsewhere [54, 63]. Integration of the partially perturbative equation (27), which is valid for W_{ac} smaller that the vibrational or vibronic dephasing rates, yields results qualitatively similar to the fifth-order treatment—again a line-narrowed vibrational resonance is not predicted [54].

Downloaded At: 17:36 21 January 2011

Typically, laser powers are too intense to be adequately described by perturbative descriptions. In this case equation (26) for CARS must be used. Assuming no feeding effects ($a=2\Gamma_{ac}/\Gamma_{cc}$ and $f=0$), contour integration gives [55]

$$\rho_{da}(\mathrm{CARS}) = W_{ca}W_{cb}W_{db} \times\left(\frac{[\Gamma_{cc}\Delta_{ca}^{*+}\Delta_{dc}\Delta_{cb}^{*+} - |W_{ac}|^2(\Gamma_{cc}\Delta_{ca}^{*+} - 2(\Delta_{ba}+\Delta_{dc})\Gamma_{ca})]}{(\Delta_{cb}^{*+}\Delta_{ba}+|W_{ac}|^2)(\Delta_{da}^{+}\Delta_{dc}-|W_{ac}|^2)(\Gamma_{cc}\Delta_{ca}^{*+}\Delta_{ca}^{+}+4\Gamma_{ca}|W_{ac}|^2)}\right.$$
$$+\frac{\mathrm{i}\sigma\{2\Gamma_{cc}\Delta_{ca}^{\mathrm{P}*}\Delta_{cb}^{\mathrm{P}*}+(|W_{ac}|^2/\Delta_{dc})[-2\Gamma_{cc}\Delta_{ca}^{\mathrm{P}*}+4\Gamma_{ca}(\Delta_{ba}+\Delta_{dc})]\}}{\Delta_{\mathrm{P}}^{+}\Delta_{\mathrm{P}}^{-}(\Delta_{ba}\Delta_{cb}^{\mathrm{P}*}+|W_{ac}|^2)(\Gamma_{cc}\Delta_{ca}^{\mathrm{P}}\Delta_{ca}^{\mathrm{P}*}+4\Gamma_{ca}|W_{ac}|^2)}$$
$$\left.+\frac{\sigma\{\mathrm{i}\Delta_{dc}(\Gamma_{\mathrm{P}}+\Gamma_{ca})(\Delta_{cb}^{*}-\Delta_{ca}^{\Gamma})+|W_{ac}|^2[-\mathrm{i}(\Gamma_{\mathrm{P}}+\Gamma_{ca})+(2\Gamma_{ca}/\Gamma_{ca})(\Delta_{ba}+\Delta_{dc})]\}}{\Gamma_{\mathrm{P}}(-\Delta_{ca}^{\Gamma-})(-\Delta_{ca}^{\Gamma+})[\Delta_{ba}(\Delta_{cb}^{*}-\Delta_{ca}^{\Gamma})+|W_{ac}|^2][\Delta_{dc}(\Delta_{da}-\Delta_{ca}^{\Gamma})-|W_{ac}|^2]}\right) \quad (44\,a)$$

where

$$\Delta_{\mathrm{P}} \equiv \frac{|W_{ac}|^2}{\Delta_{dc}} - \Delta_{dc}, \quad (44\,b)$$

$$\Gamma_{\mathrm{P}} \equiv \frac{(4\Gamma_{cc}\Gamma_{ca}|W_{ac}|^2+\Gamma_{cc}^2\Gamma_{ca}^2)^{1/2}}{\Gamma_{cc}}, \quad (44\,c)$$

$$\Delta_{ij}^{\mathrm{P}} = \Delta_{ij} + \Delta_{\mathrm{P}}, \quad (44\,d)$$

$$\Delta_{ij}^{\mathrm{P}*} = \Delta_{ij}^{*} + \Delta_{\mathrm{P}} \quad (44\,e)$$

$$\Delta_{\mathrm{P}}^{\pm} = \Delta_{\mathrm{P}} \pm \mathrm{i}\sigma \quad (44\,f)$$

$$\Delta_{ca}^{\Gamma} = \Delta_{ca} + \mathrm{i}\Gamma_{ca} - \mathrm{i}\Gamma_{\mathrm{P}}, \quad (44\,g)$$

and

$$\Delta_{ca}^{\Gamma\pm} = \Delta_{ca}^{\Gamma} \pm \mathrm{i}\sigma. \quad (44\,h)$$

In the low power limit, the three terms in equation (44 *a*) combine and it reduces to equation (40). Note that the last term in equation (44 *a*) has resonances that are not inhomogeneously broadened. They are the line-narrowed resonances expected from a nonparametric process. The resonances depend on the differences $(\Delta_{cb}^{*}-\Delta_{ca}^{\Gamma})$ and $(\Delta_{da}-\Delta_{ca}^{\Gamma})$ so their positions will shift if either of the resonances in the difference are changed. There are additional terms in the resonance denominators that reflect the dynamic Stark splittings that arise from saturation.

The changes in the line-narrowing capabilities of CARS when saturation occurs can be understood by examining the Liouville diagram for CARS in figure 3. For line narrowing to occur, at least two inhomogeneously perturbed resonances must be accessed, one to label a set of sites and the other to probe those selected sites. In addition, destructive interference between resonant and slightly nonresonant sites can destroy the line narrowing otherwise expected, as is the case for CARS in third order as expressed by equation (40). In general, nonparametric processes can be shown to have the appropriate sign differences to avoid destructive interference. In figure 3, it can be seen that higher order pathways involve the excited state as well as a number of higher-order coherences. A CARS process from an initially populated excited state (ρ_{cc}) is a nonparametric process and therefore would be expected to exhibit line-narrowing as is in fact observed. It should, however, be cautioned that fully coherent pathways must

Downloaded At: 17:36 21 January 2011

also be considered. As seen in the fifth-order treatment, interference between the various pathways led to the elimination of one line-narrowed resonance otherwise associated with an initial excited-state population.

2.7. *Relative intensities in multiresonant nonlinear mixing-mode mixing*

Multiresonant CFWM spectra are best recorded by fixing all but one resonance and monitoring the mixing signal as the remaining resonance is scanned. For molecular four-wave mixing experiments, it is common to use electronic, vibrational and vibronic resonances. We will use the symbols o, v, o', and v' in place of *a*, *b*, *c*, and *d* in the previous equations to indicate the ground, vibrational, electronic, and vibronic states involved in the mixing. Vibrational spectra are recorded by fixing the electronic and vibronic resonances. Vibronic spectra are recorded by fixing the electronic and vibrational resonances. The relative intensities in such scans are determined by the transition moments and linewidths.

In a vibronic scan, the peak intensities in the absence of pure dephasing, saturation, and inhomogeneous broadening are proportional to [64]

$$|\chi^{(3)}|^2_{\text{vibronic}} \propto \left| \frac{\mu_{v'v}\mu_{v'o}}{\Delta_{v'o}} \right|^2, \tag{45}$$

while in a vibrational scan, the peak intensities are proportional to

$$|\chi^{(3)}|^2_{\text{vibrational}} \propto \left| \frac{\mu_{v'v}\mu_{o'v}}{\Delta_{vo}} \right|^2. \tag{46}$$

These two types of spectra share a depencence on $\mu_{v'v}$ and differ only in the factors for the vibronic and vibrational resonances. In the Franck–Condon approximation, the $\mu_{v'o}$ and $\mu_{o'v}$ differ only in their signs, resulting in a mirror symmetry between the two types of scans that is analogous to the usual absorption/fluorescence mirror symmetry. There are, however, important differences between multiresonant CFWM spectra and conventional absorption and fluorescence spectra.

There are two important classes of lines that will be seen in multiresonant CFWM spectra [64]. Restricting our attention first to vibrational/vibronic fundamentals only, a vibronic spectrum will show lines corresponding to vibronic modes that correspond to different normal modes than that of the vibrational resonance. There will also be one line that corresponds to the same mode. These transitions are labelled intermode and common mode peaks respectively. Similarly, a vibrational spectrum will have intermode and common mode peaks depending on the vibronic mode resonance that was chosen.

The relative peak intensities in a standard absorption spectrum scale as

$$A_{ov'} \propto \frac{|\mu_{ov'}|^2}{\Gamma_{v'o}} \tag{47}$$

and in a relaxed fluorescence spectrum as,

$$I_{o'v} \propto \frac{|\mu_{o'v}|^2}{\Gamma_{vo}}. \tag{48}$$

These factors are closely related to the relative intensities in multiresonant nonlinear vibronic and vibrational scans, but they scale linearly with linewidth as compared with

Downloaded At: 17:36 21 January 2011

the quadratic dependence for CFWM. The linewidth difference can be eliminated by taking the following ratios [64].

$$\frac{|\chi^{(3)}|^2_{\text{vibronic}}}{A^2_{\text{ov}'}} = \left|\frac{\mu_{\text{v}'\text{v}}}{\mu_{\text{v}'\text{o}}}\right|^2 \propto \frac{\sigma_{\text{v}'\text{v}}}{\sigma_{\text{v}'\text{o}}} \tag{49}$$

and

$$\frac{|\chi^{(3)}|^2_{\text{vibrational}}}{I^2_{\text{o}'\text{v}}} = \left|\frac{\mu_{\text{v}'\text{v}}}{\mu_{\text{o}'\text{v}}}\right|^2 \propto \frac{\sigma_{\text{v}'\text{v}}}{\sigma_{\text{o}'\text{v}}}. \tag{50}$$

These ratios do not have a dependence on linewidths and they can be readily interpreted in terms of other spectroscopies. The intensities in vibronic scans relative to the square of the absorption spectrum have a similar dependence to the ratio of absorption cross-sections (σ) from a vibrational state relative to the normal absorption spectrum. Similarly, the intensities in a vibrational scan relative to the square of the fluorescence spectrum have a similar dependence to the ratio of an excited vibronic level fluorescence relative to the normal fluorescence spectrum. Thus these methods are analogous to single vibronic-level fluorescence and single vibrational-level excitation.

For relatively small geometry changes between electronic states, the common mode peaks in multiresonant nonlinear spectra will typically be enhanced over the intermode peaks [64]. An approximation for the enhancement can be obtained if the transition moments can be factored into a product of independent Franck–Condon factors for each mode. Thus, for two normal modes s and d,

$$\mu_{\text{v}'\text{v}} \propto \langle \text{v}'_\text{s}\text{v}'_\text{d}|\text{v}_\text{s}\text{v}_\text{d}\rangle = \langle \text{v}'|\text{v}\rangle_\text{s}\langle \text{v}'|\text{v}\rangle_\text{d}. \tag{51}$$

If the s vibrational mode is chosen as a constant resonance, a vibronic scan will have a resonance with the same mode in the excited electronic state, $|\text{v}'_\text{s}\rangle$, and resonances with different vibronic modes, $|\text{v}'_\text{d}\rangle$. Using equation (51) in equations (49) and (50), the intensity of the common mode peak relative to the squared absorption spectrum is

$$\left(\frac{|\chi^{(3)}|^2_{\text{vibronic}}}{A^2_{\text{ov}'}}\right)_{\text{common mode}} = \left|\frac{\langle \text{v}'|\text{v}\rangle_\text{s}}{\langle \text{o}|\text{v}'\rangle_\text{s}}\right|^2, \tag{52}$$

while the intensity of the intermode peaks relative to the squared absorption spectrum is

$$\left(\frac{|\chi^{(3)}|^2_{\text{vibronic}}}{A^2_{\text{ov}'}}\right)_{\text{intermode}} = \left|\frac{\langle \text{o}'|\text{v}\rangle_\text{s}}{\langle \text{o}'|\text{o}\rangle_\text{s}}\right|^2. \tag{53}$$

Note that the intermode intensities depend only on the Franck–Condon factors associated with the selected constant resonance (s). That is, the relative intensity of all intermode peaks scales as the squared absorption spectrum. Common mode peaks, however, will be enhanced as given the ratio of equation (52) to (53). That enhancement factor may be written [64] as

$$E_{\text{v}'\text{v}} = \left|\frac{\langle \text{v}'|\text{v}\rangle_\text{s}\langle \text{o}'|\text{o}\rangle_\text{s}}{\langle \text{v}'|\text{o}\rangle_\text{s}\langle \text{o}'|\text{v}\rangle_\text{s}}\right|^2. \tag{54}$$

Expressions for the enhancement factor can be obtained from the Franck–Condon factors in terms of the excited-state offsets, Δ, given in ground state mass normalized

Downloaded At: 17:36 21 January 2011

dimensionless units [64]. Neglecting changes in vibrational changes in vibrational frequencies between states,

$$\langle 0|0\rangle = \exp(-\Delta^2/4), \tag{55}$$

$$\langle 0|1\rangle = -\frac{\Delta}{2^{1/2}}\exp -\frac{\Delta^2}{4}, \tag{56}$$

$$\langle 1|0\rangle = \frac{\Delta}{2^{1/2}}\exp -\frac{\Delta^2}{4}, \tag{57}$$

$$\langle 1|1\rangle = \left(1-\frac{\Delta^2}{2}\right)\exp -\frac{\Delta^2}{4}. \tag{58}$$

One can therefore derive the following enhancement factors,

$$E_{1'1} = \left(1-\frac{2}{\Delta^2}\right)^2, \tag{59}$$

$$E_{2'1} = E_{1'2} = \left(1-\frac{4}{\Delta^2}\right)^2, \tag{60}$$

$$E_{2'2} = \left(1-\frac{8}{\Delta^2}+\frac{8}{\Delta^2}\right)^2, \tag{61}$$

where the subscripts label the number of quanta in each mode. These expressions are shown in figure 6. The enhancements of the common mode peak can be many orders of magnitude for small offsets.

The factorization of the total transition moment into a product of Franck–Condon factors depends on the absence of higher order mode coupling. If there are higher order mode coupling effects such as Herzberg–Teller or Duschinsky coupling, the intermode

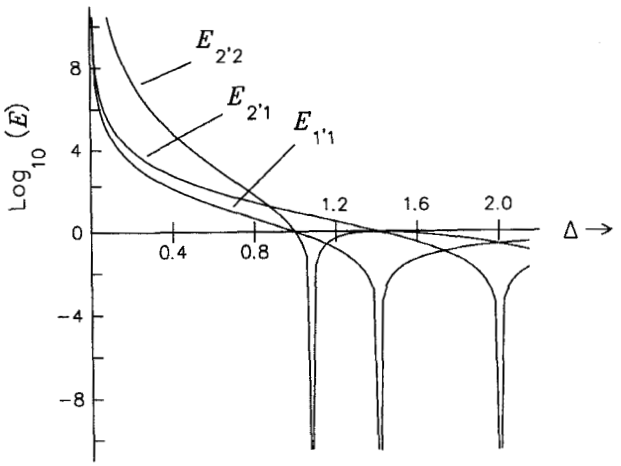

Figure 6. Common mode enhancement factors as a function of the excited electronic state potential well offset (Δ) for a Franck–Condon system. The zero point r.m.s. amplitude on the scale of the horizontal axis (mass normalized ground state dimensionless coordinates) is 0·71.

Downloaded At: 17:36 21 January 2011

peak relative intensities will deviate from the predictions of the squared absorption spectrum and in general there will be an enhancement for those modes as well. In this way, the deviations can be used as a sensitive measure of mode coupling (64–66).

3. Experimental

3.1. *Instrumental concerns*

The block diagram of the typical apparatus required for multiresonant nonlinear spectroscopy is shown in figure 7. A XeCl excimer laser (308 nm) is used to excite three tunable dye lasers. Each laser consists of a side-pumped, Littrow configuration oscillator and a single preamplifier which give combined efficiencies of $\approx 5\%$ and pulse energies of up to 1 mJ. The pulse widths are 5 ns f.w.h.m. and the bandwidths are typically 0·5–1 cm^{-1} f.w.h.m. Each laser is sent through a weakly expanding telescope to adjust its divergence so that the three beams can be brought to a common focus.

The beams are passed through filters or simple four prism monochromators to spectrally isolate the lasing wavelength from broadband amplified spontaneous emission. The four prism monochromators have two pairs of prisms set for subtractive dispersion [67]. A knife edge placed after the first pair passes the laser but blocks interfering wavelengths. Lenses are placed before and after the prisms to focus the light on the knife edge and recollimate the beam. The second pair of prisms produces an opposing translation so the beam is not deviated or translated after passing through all four prisms. This simple arrangement provides 10^5 rejection, 300 cm^{-1} from the laser line [53].

Phase matching is accomplished by spatially separating the beams as they are incident on the focusing lens before the sample. The single positive lens focuses the beams to a common 50–200 μm waist at the sample position. The samples can be cooled to ≈ 2 K by direct immersion in a pumped liquid helium dewar. The directional mixing signal is imaged on the entrance slit of a 0·85 m double monochromator that is usually used with wide slits to give a ≈ 10 cm^{-1} bandpass. The signal is then measured with a standard photomultiplier tube. The photomultiplier signal is sent to a 100 kHz bandwidth current-to-voltage converter. The slow bandwidth allows sufficient delay in the measurement to avoid radio frequency interference from the excimer laser. The resulting voltage signal is measured by a gated boxcar integrator. The signal from the boxcar is sent to an analogue-to-digital converter interfaced by a CAMAC system to a microcomputer.

Computer control of the entire system is important in order to meet the synchronization requirements for the multiresonant experiments. The computer is capable of scanning each of the dye lasers and the monochromator [67]. The wavelength of each laser is recorded with optical encoders on the lead screws. Absolute wavelength calibration of the encoders is achieved by a commercial Fizeau interferometer wavemeter that records the fringe pattern from a coated wedge with a diode array detector. Specialized software [54] was required to signal average in a statistically valid manner in order to obtain reliable measurements under the pulsed conditions of this experiment. The scanning must always be performed in a single direction to obtain the necessary reproducibility in the experiment. Separate calibrations are performed using the optogalvanic effect with a Fe–Ne hollow cathode lamp to have an independent check on the proper operation of the wavemeter. The monochromator was also calibrated with the hollow cathode lamp. The calibration is automated to make measurements across the entire range of spectral scans and the data are fitted to a sum of a linear function and a series of sinusoids that mirrors periodic

Downloaded At: 17:36 21 January 2011

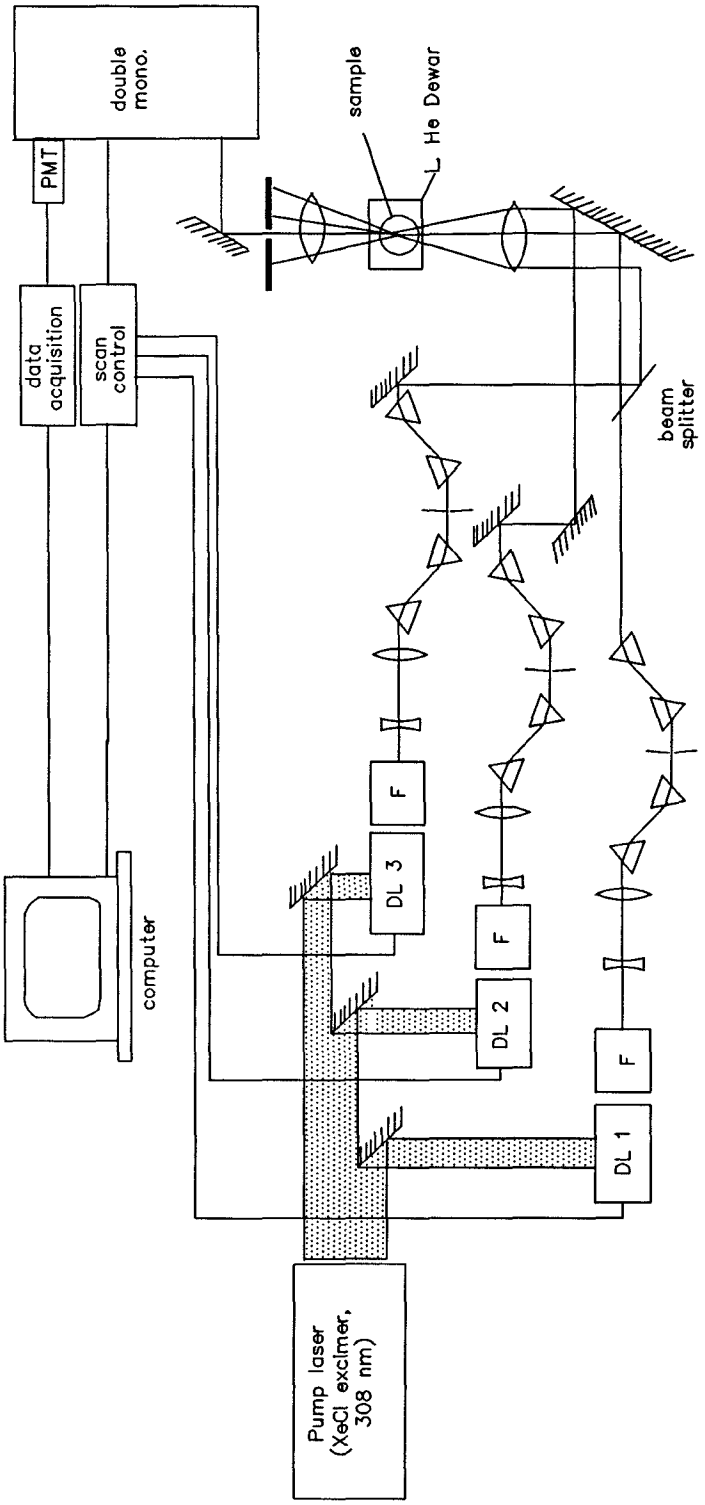

Figure 7. Block diagram of instrumental system for three-laser coherent four-wave mixing: DL = dye laser; PD = photodiode; BS = beamsplitter; F = filter.

Downloaded At: 17:36 21 January 2011

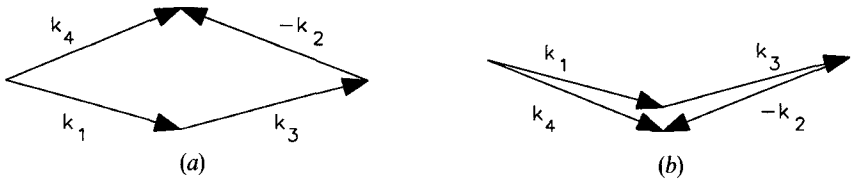

Figure 8. Coplanar phase matching diagrams for multiresonant CFWM giving an output signal at frequency $\Omega_4=\Omega_1-\Omega_2+\Omega_3$.

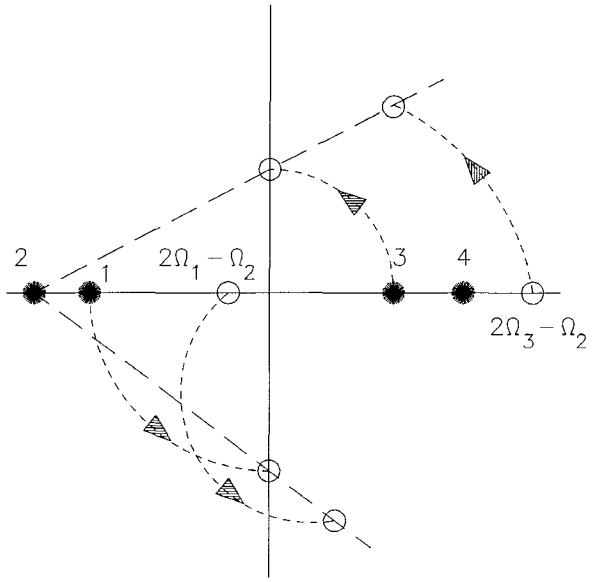

Figure 9. Three dimensional phase matching geometries for multiresonant CFWM. The points along the horizontal axis represent laser and signal beams for coplanar phase matching (see figure 8), as viewed from behind the sample. The open circles represent interfering two laser signals. The dashed arcs show the effect of rotating the $\boldsymbol{k}_1$ and $\boldsymbol{k}_2$ wavevectors about the line defined by $\boldsymbol{k}_1+\boldsymbol{k}_3$. The two laser signals are constrained to the lines connecting the $\boldsymbol{k}_1$ and $\boldsymbol{k}_2$ or $\boldsymbol{k}_3$ and $\boldsymbol{k}_2$ points. For a 90° rotation, note that both the Ω_3 laser and the signal at $2\Omega_3-\Omega_2$ have moved away from the three-laser signal, allowing better discrimination between signals.

irregularities in the lead screw. These procedures are required to meet the $\approx 0{\cdot}5\,\mathrm{cm}^{-1}$ resolution requirement dictated by the bandwidths of the lasers.

Three phase-matching geometries are typically used in the multiresonant experiments. The fundamental phase matching relationship is

$$\boldsymbol{k}_4=\boldsymbol{k}_1-\boldsymbol{k}_2+\boldsymbol{k}_3. \tag{62}$$

for experiments where the output frequency is $\Omega_4=\Omega_1-\Omega_2+\Omega_3$. For many experiments, it is convenient to use a coplanar geometry for which there are two solutions to equation (62), as shown in figure 8. The choice between the two is determined by which of the lasers has the nearest frequency to the output. The closer the frequencies, the greater the angular separation desired to eliminate scattering interference.

In some cases, it is helpful to use a three dimensional phase matching, particularly if interference from output signals at $\Omega_4=2\Omega_1-\Omega_2$ or $\Omega_4=2\Omega_3-\Omega_2$ is a problem. This interference is minimized by using the phase matching geometry depicted in figure 9.

Downloaded At: 17:36 21 January 2011

This figure shows the positions of the four beams in a plane perpendicular to each. An infinite number of solutions are possible which correspond to rotations of the plane defined by $\boldsymbol{k}_1$ and $\boldsymbol{k}_3$ relative to that defined by $\boldsymbol{k}_4$ and $\boldsymbol{k}_2$ about the line $\boldsymbol{k}_1+\boldsymbol{k}_3$. Since the two laser signals stay in the plane defined by $\boldsymbol{k}_1$ and $\boldsymbol{k}_2$ or $\boldsymbol{k}_3$ and $\boldsymbol{k}_2$, the three laser signal becomes well separated from them.

3.2. *Experimental implementation*

The basic CFWM experiment is conceptually simple but there are a number of common difficulties that arise in practice. Four factors are particularly crucial: (1) accurate and precise frequency measurements, (2) correct phase matching, (3) overlap of the beams both spatially and temporally, and (4) correct sample positioning relative to the beam overlap region.

There can be subtle experimental problems that can prevent these four conditions from being fulfilled. For example, it is common to have a wedged output window on a dye laser oscillator to prevent etalon effects. Scanning the laser will cause the pathway through the wedge to change because of the wedge's dispersion. If the laser is aligned to retroreflect light back into the cavity from the inside surface of the output wedge, the beam leaving the dye laser will change direction as a function of wavelength. This change in pointing direction will cause the phase matching and beam overlap to change during the scan. If the laser is aligned to retroreflect from the outside surface, the beam leaving the dye laser will remain fixed in direction but the path through the oscillator cavity will change with wavelength. If the changes are occurring in the plane of dispersion, only the wavelength calibration of the dye laser will be affected and this can be corrected for by the calibration procedure.

Downloaded At: 17:36 21 January 2011

In multiresonant CFWM, it is desirable to keep all but one resonance fixed as a scan of the remaining resonance is performed. For the different four-wave mixing methods shown in figure 2, the system requirements change for scans of different resonances. In any fully resonant scan, however, there are always two frequency elements that must be changed in synchronization. For CARS, a vibrational scan requires changing lasers at Ω_2 and Ω_3 in such a way that the vibronic resonance at $\Omega_1-\Omega_2+\Omega_3$ does not change. Thus, both Ω_2 and Ω_3 must increase at the same rate. For a vibrational scan in MENS, the laser at Ω_3 must be scanned in synchronization with the monochromator while the other lasers remain fixed in frequency. In all cases, it is important that the synchronization be better than the widest bandwidth so that artifacts from tracking errors are not introduced. One of the lasers can be broadened by decreasing the magnification of the telescope in the oscillator if necessary in order to eliminate errors in tracking. The resolution of the system will not be degraded if the bandwidth of the other frequency elements (including the monochromator) remain narrow because the condition $\Omega_4=\Omega_1-\Omega_2+\Omega_3$ constrains the range of frequencies that is actually measured.

It is important to realize that an experiment where two resonances are always maintained during a scan will probably have a background that is determined by those two resonances and not by the nonresonant background of the sample. Peaks appear in the spectrum because the third resonance raises the mixing efficiency by an additional multiplicative factor. The triply resonant condition at the peaks in typical scans provides strong discrimination against the nonresonant background limitations. One can therefore tolerate lower concentration levels than in singly or doubly resonant experiments.

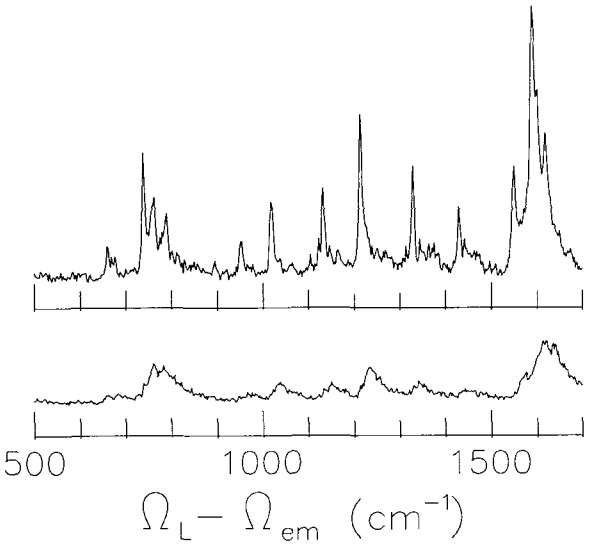

Figure 10. Fluorescence spectra of OEP in PMMA at 2 K when the excitation laser is slowly scanned (top spectrum) and when it is fixed (lower spectrum). Ω_L is the laser frequency and Ω_{em} is the emission frequency.

Downloaded At: 17:36 21 January 2011

Maintenance of two constant resonances can cause hole burning in an inhomogeneously broadened transition of a sample, depending on the pulse energies of the lasers, the length of time required for spectra and the sample hole burning efficiency. It is possible to eliminate the hole burning effects if the other resonances are slowly scanned [68]. In such a scan, the spectroscopy is actually sampling different sites within the inhomogeneous width. If the scanning range is small in comparison with the inhomogeneous width, there will usually not be distortions in the spectra since the different sites within an inhomogeneously broadened line have the same vibrational and vibronic energies relative to the vibrationless level. For example, in a vibrational scan for fully resonant CARS, $\Omega_{o'o}$ can be slowly scanned across the inhomogeneously broadened electronic transition while $\Omega_{o'v}$ and $\Omega_{v'v}$ were synchronously scanned much more rapidly with the constraint that $\Omega_{v'v} - \Omega_{o'v}$ be held constant. The sites resonant with $\Omega_{o'o}$ would be constantly changing but the vibronic resonances of the resonant sites would be constant since $\Omega_{v'v} - \Omega_{o'v}$ is constant.

An example of this procedure for line narrowed fluorescence spectroscopy is shown in figure 10. In this experiment, octaethylporphine (OEP) in polymethylmethacrylate (PMMA) is excited and the line narrowed fluorescence emission spectrum was recorded [68]. The lower spectrum was recorded with the excitation laser (Ω_L) fixed while the upper spectrum was recorded with the excitation laser scanned slowly. Vibrational features fall at constant differences between the laser frequency and the fluorescence frequency. The lower spectrum is broader because the sites associated with the sharp lines have been burned away. The upper spectrum remains sharp because the slow scan constantly exposes new sites to the laser resonance at a rapid enough rate that hole burning is negligible.

3.3. *Spectral interpretation*

There are two important sources of artifacts in multiresonant spectra: detection of competing four-wave mixing processes, and multiple resonances from different

combinations of the laser frequencies. In a three-laser experiment that measures the signal at $\Omega_1-\Omega_2+\Omega_3$, there will be interference from the output signals at $2\Omega_1-\Omega_2$ and $2\Omega_3-\Omega_2$ when $\Omega_1=\Omega_3$ in a scan of either Ω_1 or Ω_3. Such a scan will have an increased intensity at this position and will be interpreted as a peak if one is not cautious. This peak has been called the degenerate peak and it can be useful as a marker for the position where $\Omega_1=\Omega_3$. For example, if a vibrational resonance is located at $\Omega_1-\Omega_2$, a vibronic CARS scan will include the degenerate peak at $\Omega_3-\Omega_2=\Omega_1-\Omega_2$ that marks the position of the vibrational resonance so it can be used for comparison with the vibronic features at other values of $\Omega_3-\Omega_2$. The degenerate peak can be eliminated by the three-dimensional phase matching methods described previously.

Unexpected peaks can sometimes appear in a spectrum that has been designed around a particular set of resonance conditions. Figure 11 shows a series of resonances that can be associated with different mixing methods. For example, in a CARS experiment, lasers with frequencies Ω_1 and Ω_2 can be chosen to match the electronic and vibrational resonances shown in figure 11 (*a*). A vibronic scan where Ω_3 and Ω_4 are changed will be expected to show triply resonant vibronic features with energies given by $\Omega_3-\Omega_2$ relative to the electronic origin. However, vibrational features can also appear in the spectrum when $\Omega_3-\Omega_2$ matches vibrational energies. The resonances for this process are shown in figure 11 (*b*). The difference from figure 11 (*a*) is the interchange in the roles for Ω_1 and Ω_3. The new peaks (often termed '321' peaks) should be smaller because they will generally be only singly resonant. They can appear in spectra when the modes are particularly strong or if accidental multiply resonant conditions exist. 321 resonances are particularly important in experiments with large inhomogeneous broadening because the multiplicity of sites increases the chances of multiply resonant conditions.

Downloaded At: 17:36 21 January 2011

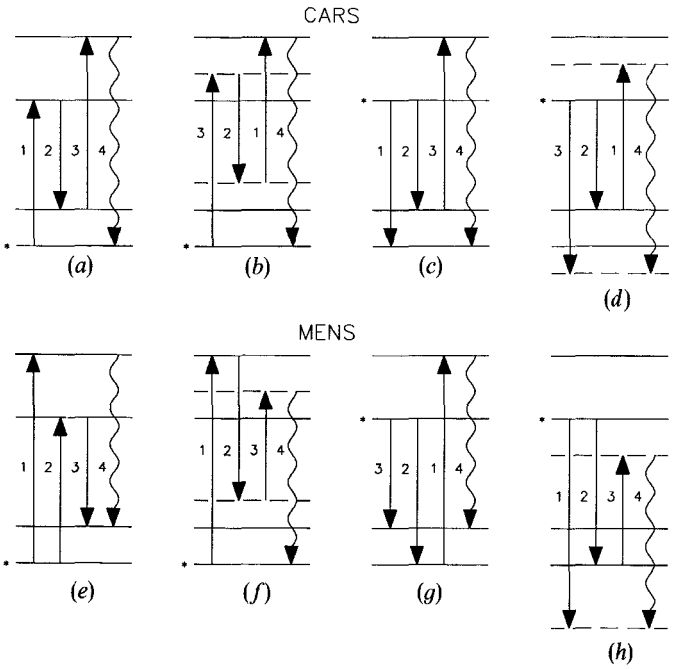

Figure 11. Different CFWM processes that can occur for CARS (*a–d*) or MENS (*e–h*). The asterisks label the initial state in each diagram. The diagrams in the last two columns show processes arising from excited state populations.

One can also have unexpected resonances from excited state four wave mixing. An example is shown in figure 11 (*c*, *d*). An electronically excited population undergoes four-wave mixing by a nonparametric process to produce an output frequency identical to CARS. Vibrational and vibronic resonances can both appear at either $\Omega_1 - \Omega_2$ or $\Omega_3 - \Omega_2$ depending upon which process occurs. There are many other resonance processes that could also be drawn and these may be important under special circumstances.

Similar considerations are important for interpreting other multiresonant nonlinear spectra. A second example is shown in figure 11 (*e–h*) for MENS experiments. Although many of the same considerations apply to this case, it is interesting to note that the case where the roles of Ω_1 and Ω_3 are interchanged is the MEPS process shown in figure 11 (*f*). Whereas vibronic resonances fell at particular values of $\Omega_1 - \Omega_2$ in the process for figure 11 (*e*), there can also be vibrational resonances from the MEPS process of figure 11 (*f*) at $\Omega_1 - \Omega_2$.

4. Multiresonant two-laser CARS experiments

Multiresonant two laser CARS experiments were pioneered by Hochstrasser and coworkers [14] as described in the introduction. The typical features that one will observe are shown in figure 12. It is generally not possible to perform fully resonant

Downloaded At: 17:36 21 January 2011

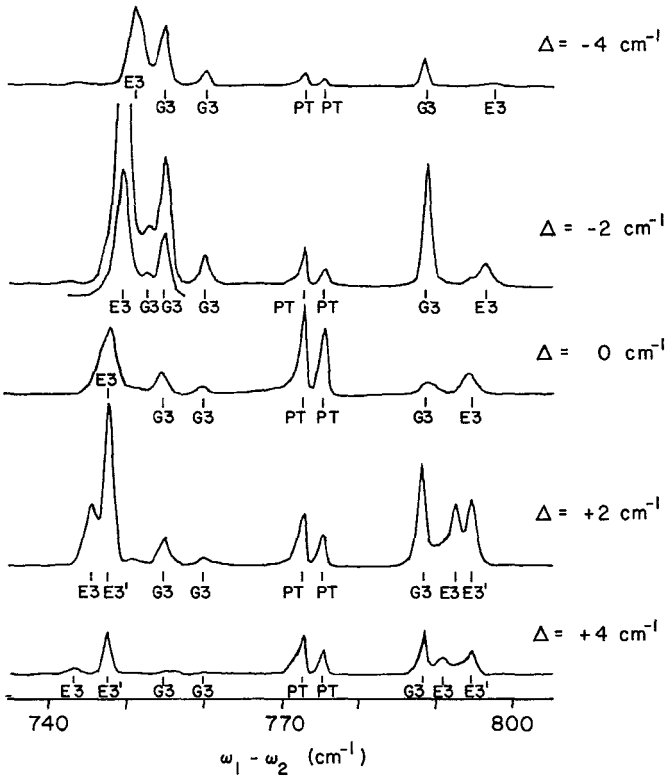

Figure 12. Two laser CARS spectra of pentacene doped p-terphenyl crystals at 2 K for a series of different detunings ($\delta = \Omega_1 - \omega_{o'o}$) from the electronic origin of pentacene in site 3. The G3, E3, E3′, and PT label transitions of site 3 assigned to ground state vibrational states, excited vibronic states, vibronic transitions from excited populations, and p-terphenyl transitions.

experiments with two lasers since by definition, $\Omega_{o'o}=\Omega_{v'v}$, nor is it possible to scan one resonance independently of the others. In figure 12, the output signal at $\Omega_{v'o}=2\Omega_{o'o}-\Omega_{o'v}$ is monitored as a function of $\Omega_{o'v}$. The results are plotted as a function of $\Omega_{o'o}-\Omega_{o'v}$. The sample is pentacene doped crystals of p-terphenyl at 2 K. In this crystal, there are four crystallographically inequivalent pentacene sites with different electronic origins. The spectra in figure 12 were taken with $\Omega_{o'o}$ near the electronic origin of site 3 ($\omega_{o'o}=17005{\cdot}7\,\mathrm{cm}^{-1}$) [69]. A series of spectra were taken for different detunings ($\delta\equiv\Omega_{o'o}-\omega_{o'o}$) of $\Omega_{o'o}$ from the electronic origin.

There are three strong vibrational (labelled by G3) and two vibronic pentacene features (labelled by E3) that arise from the normal CARS process shown in figure 11 (*a*). The vibrational features do not change in their $\Omega_{o'o}-\Omega_{o'v}$ position as $\Omega_{o'o}$ is changed, but the vibronic features all shift. Hochstrasser and coworkers have used this shift to classify transitions [14–17]. The relative intensities of the peaks change during these detuning experiments because the vibrational and vibronic detunings are changing. As the E3 lines approach the G3 lines, the peak intensities increase because there are both vibrational and vibronic enhancements. The E3 and G3 lines overlap when the energy difference between the vibronic and vibrational modes matches the detuning ($\omega_{v'o'}-\omega_{vo}=\delta$), and the relative peak intensity is a local maximum. The peaks labelled PT in the figure are the vibrational lines from the p-terphenyl host crystal. There are several new features (labelled E3′) that appear for positive detunings from each site that are associated with excited state CARS processes like that shown in figure 11 (*d*). Large excited-state populations would be expected for positively detuned $\Omega_{o'o}$ values since the pentacene phonon sidebands can be excited.

The situation becomes more complex when sites 1 and 2 are studied because they have almost identical excited electronic state energies. The electronic origin of site 1 is at $16883{\cdot}0\,\mathrm{cm}^{-1}$ while that for site 2 is at $16886{\cdot}8\,\mathrm{cm}^{-1}$. CARS spectra are shown in figure 13 for a series of $\Omega_{o'o}$ detunings across this region [69]. The vibrational and

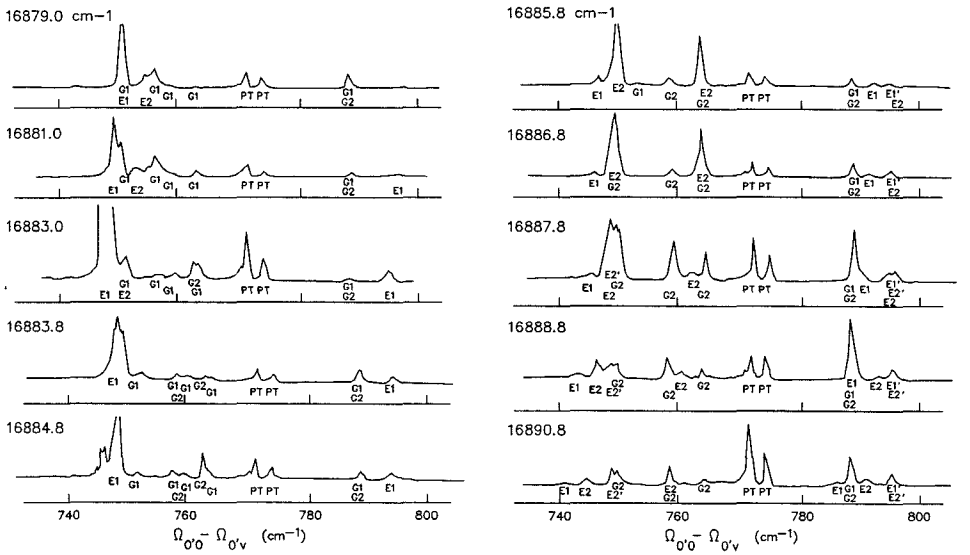

Figure 13. Two-laser CARS spectra of pentacene doped p-terphenyl crystals at 2 K for a series of detunings from the electronic origin of pentacene in sites 1 and 2. The labelling is identical to figure 12.

Downloaded At: 17:36 21 January 2011

vibronic features of sites 1 and 2 are labelled by G1, G2, E1, or E2 in analogy to the labelling for site 3. One can see the same shifting position of the vibronic features throughout the range of detunings. When the vibrational and vibronic features overlap, the total peak intensity is particularly large because of the simultaneous vibrational and vibronic resonance enhancements. This effect is particularly clear for the site 1 lines around 790 cm^{-1}. The peaks overlap in the $\Omega_{o'o} = 16888{\cdot}8\ cm^{-1}$ spectrum and the peak intensity from these site 1 lines is larger than any of the site 2 transitions even though $\Omega_{o'o}$ is far from the site 1 electronic resonance at $16883{\cdot}0\ cm^{-1}$.

It is also clear from figure 13 that resonance with the electronic transition of either site causes a large enhancement in all of their vibrational and vibronic features. The spectra for $\Omega_{o'o} = 16883\ cm^{-1}$ are dominated by site 1 transitions while the spectra for $\Omega_{o'o} = 16886{\cdot}8\ cm^{-1}$ are dominated by site 2 transitions. For those spectra, there will be double resonance enhancement of lines from the electronic and either a vibrational or vibronic resonance. There are examples where lines from one of the sites appears in a spectrum that is dominated by the other site. These exceptions occur for the cases where there is a double resonance from vibrational and vibronic states whose positions overlap such as the site 1 lines in the $16888{\cdot}8\ cm^{-1}$ spectrum discussed above.

In addition to the normal vibrational and vibronic features, there are also examples of lines from excited electronic state populations. These lines are labelled as E1′ and E2′. They appear only when the $\Omega_{o'o}$ energy exceeds the $\omega_{o'o}$ energy of a site and they remain at fixed positions of $\Omega_{o'o} - \Omega_{o'v}$ for different values of $\Omega_{o'o}$.

Downloaded At: 17:36 21 January 2011

5. Multiresonant three-laser nonlinear spectroscopy

5.1. *Component selection*

Site-selective laser spectroscopy has become a standard method for studying multicomponent systems. Its application to the four-site pentacene doped p-terphenyl system is illustrated in figure 14 [59]. The top spectrum shows the composite pentacene fluorescence from sites 1 and 2. If the electronic origin of site 1 is excited, the middle spectrum results. It contains only transitions from site 1 despite the presence of the site 2 electronic origin $3{\cdot}8\ cm^{-1}$ away. The bottom spectrum is the fluorescence from selective excitation of the site 2 origin.

These spectra should be compared with the site-selective three-laser CARS spectra of the same system shown in figure 15. The single site fluorescence spectra of each site are shown at the top while the vibrational CARS scans for $\Omega_{o'o}$ resonant with each site are shown on the left panel for site 1 and the right panel for site 2. The successive spectra are obtained using the different vibronic resonances indicated. The same vibrational features are seen in these nonlinear spectra as were seen in the site selective fluorescence experiment. There is the same high degree of site selection despite the proximity of the two electronic origins.

The strong component selectivity would not be expected from the normal treatment of nonresonant Raman spectra where a sum over all electronic states must be done to determine the polarizability. A detuning of $3{\cdot}8\ cm^{-1}$ would have little effect if the polarizability had important contributions from many electronic states. The strong selectivity demonstrated in figure 15 demonstrates that only the S_1 state of pentacene has an appreciable contribution to the nonlinear Raman polarizability.

These spectra also show the strong differences between two laser experiments where two resonances are always probed in a scan and three laser experiments where a single resonance can be studied. For example, the spectra in figure 13 are complex and the

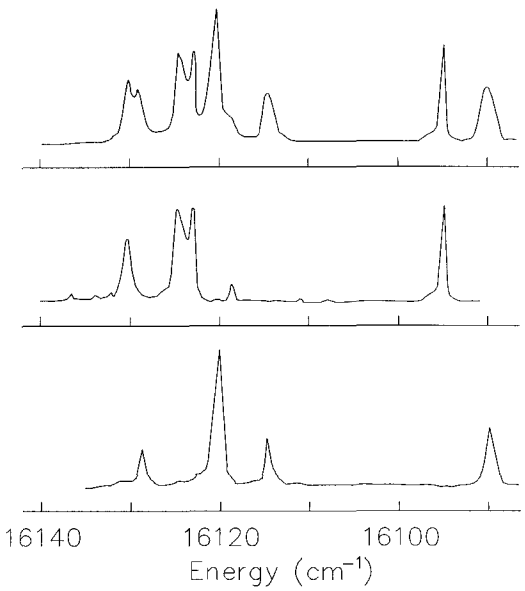

Figure 14. Fluorescence emission spectra of pentacene doped p-terphenyl crystals at 2 K. The top spectrum is the fluorescence from sites 1 and 2 while the second and third spectra are obtained by selective excitation of site 1 and 2, respectively.

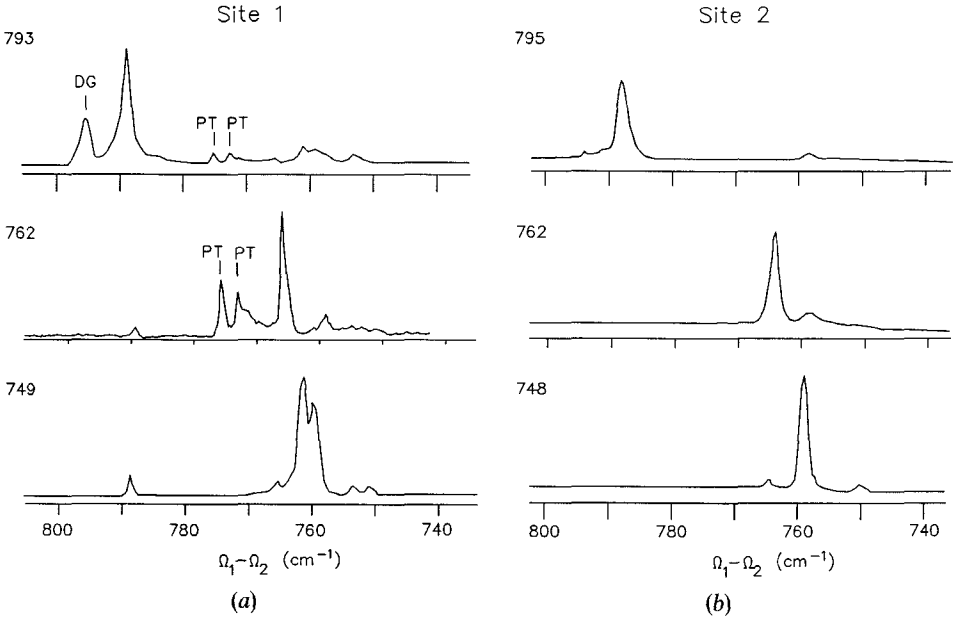

Figure 15. Vibrational three-laser CARS scans for site 1 (*a*) and site 2 (*b*) of pentacene doped p-terphenyl crystals at 2 K. The electronic resonance has been set for either site 1 or 2 while the vibrational resonance has been fixed on the mode indicated by its frequency in cm^{-1} in each spectrum. The labels PT and DG indicate the p-terphenyl and degenerate lines.

Downloaded At: 17:36 21 January 2011

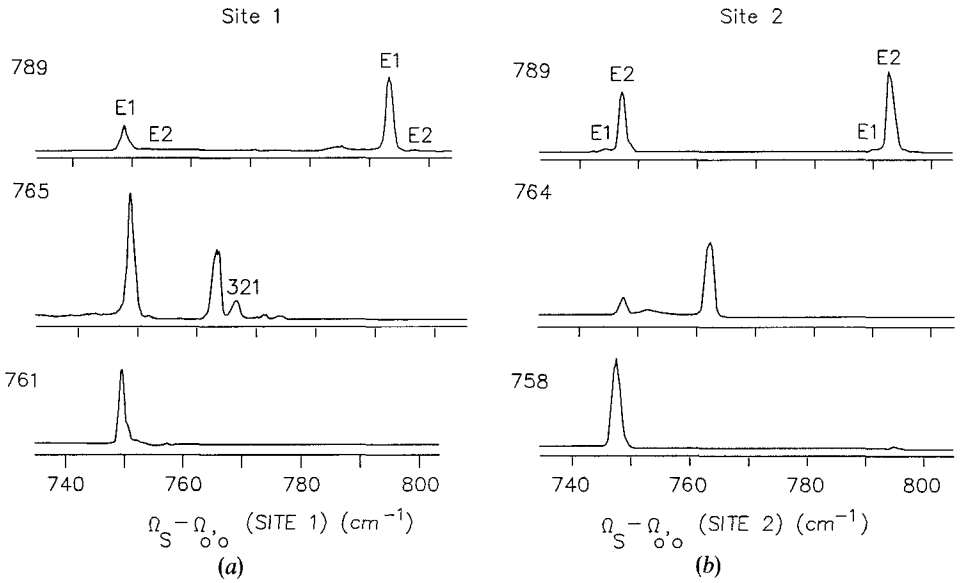

Figure 16. Vibronic three laser CARS scans for site 1 (*a*) and site 2 (*b*) of pentacene doped p-terphenyl crystals at 2 K. The electronic resonance has been set for either site 1 or 2 while the vibronic resonance has been fixed on the mode indicated with each spectrum. The 321 label indicates a line associated with a CARS resonance such as shown in figure 11 (*b*).

Downloaded At: 17:36 21 January 2011

assignment of peaks is tedious. Both vibrational and vibronic features are important and it is possible to have important contributions from the nonselected site because of double resonance enhancement between vibrational and vibronic states. The relative intensities in a series of spectra like figure 13 are difficult to understand as well because the relative enhancements from vibrational, electronic, and vibronic enhancements are changing. In three laser experiments, these complications are strongly discriminated against. Vibronic features dominate vibronic scans and vibrational features dominate vibrational scans. Transitions from the nonselected site are strongly discriminated against because such peaks would lack the triple resonance that a selected site possesses. All but the scanned resonance are being maintained at constant values.

The relative intensities in the site selective CARS spectra of figure 15 are quite different from the site selective fluorescence spectra and they are strongly dependent on the selection of the vibronic resonance used for the spectrum [62, 70]. There is a large enhancement of the vibrational common mode associated with the vibronic resonance that is held constant.

Figure 16 shows the complementary vibronic scans to figure 15 for each site [70]. The vibronic features seen in the spectra fall at the frequencies chosen as constant resonances for the spectra in figure 15. The site discrimination is again seen in this series of spectra. The relative line intensities are also dependent on the vibrational resonance that is being held constant. There is a large enhancement of the common vibronic mode associated with the selected vibrational resonance.

5.2. *Normal mode selection and mode coupling effects*

The strong dependence of the nonlinear vibrational and vibronic spectra in figures 15 and 16 on the choice of the mode for the constant resonance can be particularly useful in understanding the relationships between vibrational and vibronic modes. We

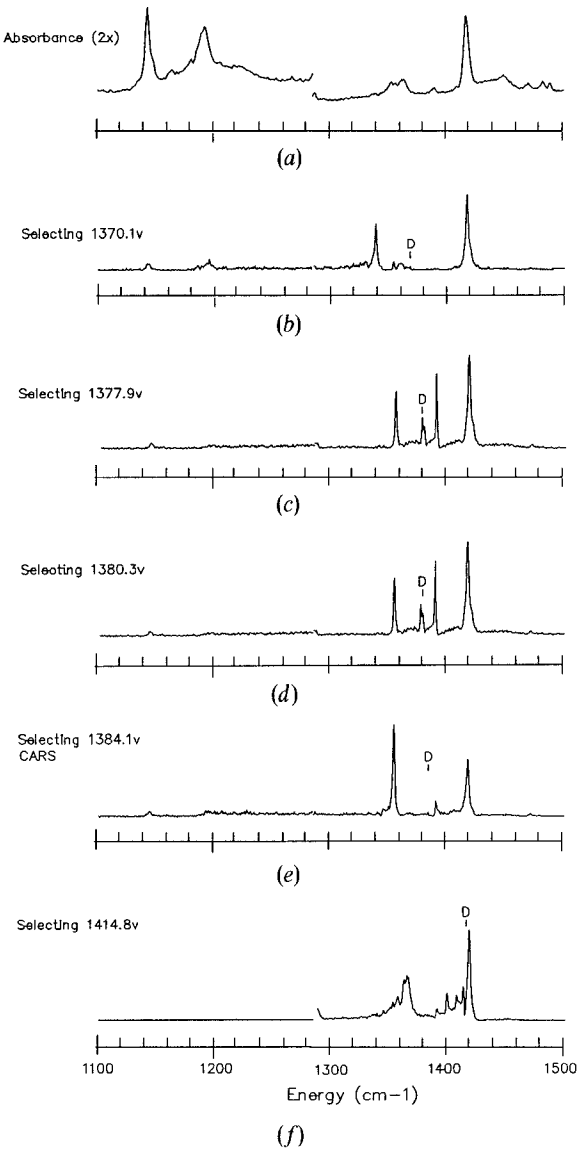

Figure 17. Three laser CARS vibronic spectra of pentacene doped benzoic acid at 2 K. Each spectrum corresponds to the selection of a different vibrational resonance as indicated in each spectrum. The D labels the degenerate position in each scan. The absorption spectrum is shown on the top for comparison.

have seen earlier how the vibrational scans are closely related to single vibronic level fluorescence spectra and how vibronic scans would be related to single vibrational level excitation spectra.

Figure 17 shows an example of how the multiresonant CFWM spectra can be used to map out the similarities (and differences) of normal modes between different electronic states [65]. The top spectrum (*a*) shows the adsorption spectrum of pentacene doped benzoic acid crystals at 2 K in the 1100–1600 cm^{-1} range. The lower spectra (*b–f*) show the vibronic three-laser CARS spectra over the same region with

Downloaded At: 17:36 21 January 2011

different choices of the vibrational resonances as indicated in each spectrum. The $\Omega_{o'o}$ laser is tuned to resonance with $\omega_{o'o}$ for all the spectra.

Comparisons of the CARS spectra show that there are particular transitions that are selectively enhanced in each of the spectra. The 1419·0 cm^{-1} vibronic line is largest in the spectrum where the 1377·9 cm^{-1} vibrational line was selected. These two lines are therefore assigned to the same vibrational normal mode. Similarly, the common mode in each of the other spectra can be picked out by identifying the transition that has been enhanced by the largest amount. As discussed in the theory section, the comparison is based on the intensity a transition would have had if the relative intensities scale as the square of the absorption spectrum assuming there is no common mode enhancement. For the 1370·1, 1377·9, 1380·3, 1384·1, and 1414·8 cm^{-1} vibrational resonances, the corresponding vibronic modes are assigned to the 1339·7, 1419·0, 1391·0, 1354·6, and 1364·4 cm^{-1} resonances, respectively. There is also a peak in the spectra labelled 'D' at the energy of the vibrational mode chosen for the constant resonance. This peak is the degenerate peak discussed in the experimental section. It is an artifact which appears when $\Omega_{o'o}=\Omega_{v'v}$.

There are other important lines in many of the spectra in figure 17 that are enhanced to a lesser degree than the common-mode transition. These lines are assigned to modes that are coupled to the mode chosen for the constant resonance. The assignments for coupling are summarized in figure 18 where the fluorescence and excitation spectra of

Downloaded At: 17:36 21 January 2011

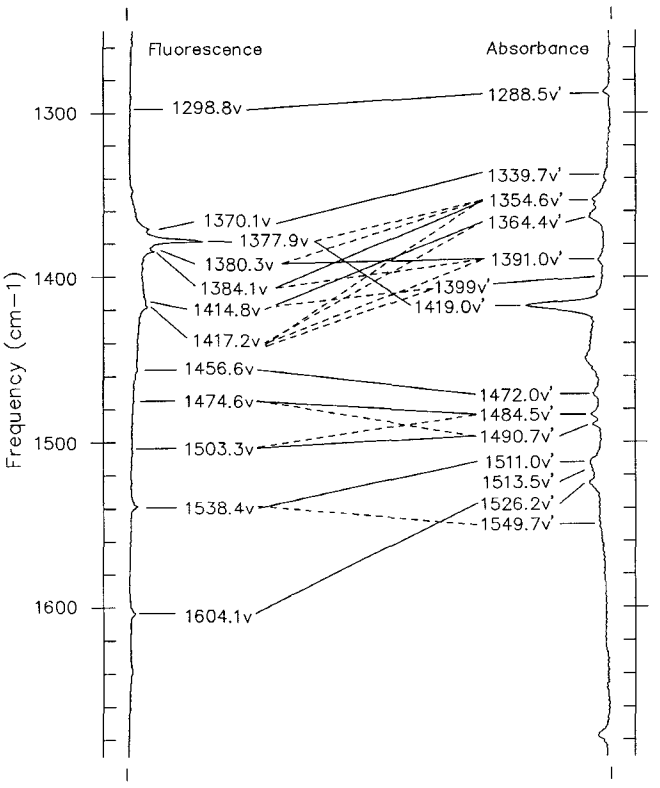

Figure 18. Summary of the correlations between the vibrational states seen in the fluorescence spectrum of pentacene doped benzoic acid crystals at 2 K and the vibronic states seen in the absorption spectrum. Solid lines connect common modes and dotted lines connect coupled modes.

the sample are presented along with solid lines connecting the common modes and dotted lines indicating the coupled modes.

One should note that the large enhancements in figure 17 can be used to distinguish lines that are not resolved or to enhance lines that are very weak [71]. For instance, the 1339·7 cm^{-1} line is not visible in the absorption spectrum but it is quite strong in the 1370·1 cm^{-1} selected spectrum. Similarly, the two lines at 1354·6 and 1364·4 cm^{-1} are overlapped in the absorption spectrum but are easily distinguished in the 1384·1 and 1414·8 cm^{-1} spectra.

A detailed mode-coupling analysis of the pentacene CFWM spectra has shown that Herzberg–Teller and Duschinsky coupling are important for many of the modes [64–66]. In addition, there are a number of examples where phonon assisted Duschinsky coupling and phonon induced mode mixing appear to be important. These mixings occur when two vibrational levels are separated by the energy of a lattice phonon.

5.3. *Line narrowing with multiresonant nonlinear spectroscopy*

Line narrowing with multiresonant nonlinear spectroscopy was reported by Riebe and Wright [53, 72] in pentacene doped benzoic acid crystals, codoped with p-terphenyl to introduce a controlled amount of inhomogeneous broadening. The line narrowing was accomplished by tuning the electronic resonance to different positions within the inhomogeneous width of the electronic transition. This resonance was fixed on the 260 cm^{-1} fundamental of pentacene. Both CARS and MENS spectra were taken in order to compare their line narrowing capabilities.

The line-narrowed CFWM spectra are shown in figure 19 along with the inhomogeneously broadened absorption profile of the vibronic band. A series of spectra are presented for different positions of $\Omega_{o'_0}$ within the inhomogeneously broadened origin band. The linewidths of the narrowed transitions are limited by the bandwidths of the lasers. The position of the narrowed resonance shifts to different positions within the inhomogeneous envelope because different sites are selected by the electronically resonant laser. This effect was predicted by equations (41) and (43) for the line-narrowed peaks.

Note that line-narrowing behaviour was observed for both CARS and MENS. As discussed in the theoretical section, line-narrowing cannot occur for a parametric process like CARS unless higher order effects become important. Under saturation conditions, there are other pathways for generating coherence that are nonparametric processes which can be line-narrowed. It is these higher order effects that are responsible for the narrowed spectra in the CARS experiments of figure 19.

These results have recently been extended to amorphous systems with large inhomogeneous broadening [55]. Such systems are more representative of samples of practical interest. The primary effect of large inhomogeneous broadening is to introduce more ways that multiple resonances can occur during a spectral scan because of the broad range of sites that are present.

Perylene doped PMMA samples were used as a model for these studies [55]. The 2 K absorption and fluorescence spectra are shown in figure 20. The origin is at $22650 \pm 50\,cm^{-1}$ and there are strong vibrational and vibronic features near 1400 cm^{-1}. The inhomogeneous width is estimated to be 420 cm^{-1}. Laser-induced, fluorescence line narrowing can be used to selectively excite sites within the inhomogeneous width of the $o \rightarrow o'$ transition to obtain the spectrum shown in figure 21. One can thereby resolve the vibrational features that were hidden by the

Downloaded At: 17:36 21 January 2011

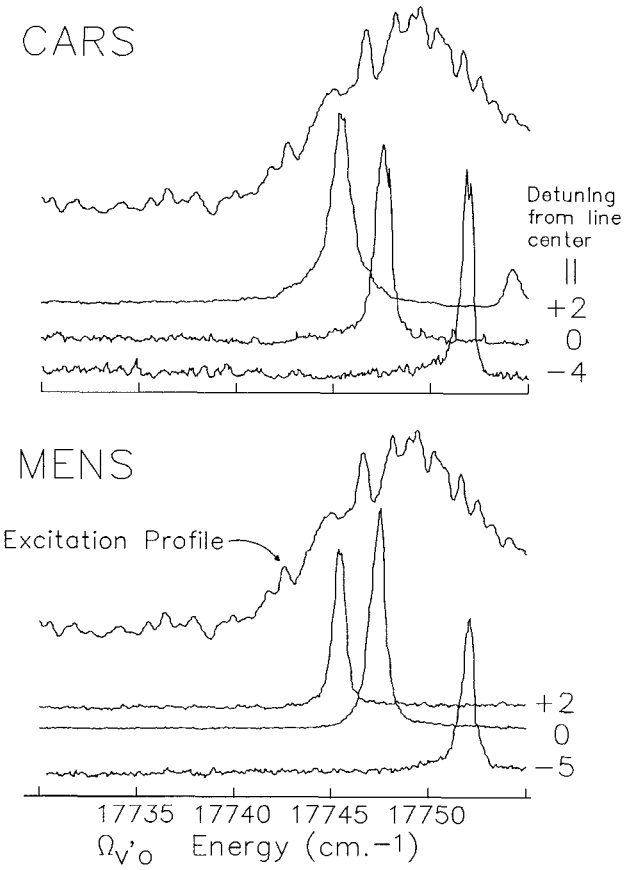

Figure 19. Three-laser CARS and MENS spectra of pentacene doped benzoic acid with 2% p-terphenyl added to introduce inhomogeneous broadening. The three nonlinear spectra shown for each case correspond to different positions of $\Omega_{o'o}$ within the inhomogeneous width of the o↔o′ transition. The inhomogeneously broadened absorption line profile of the vibronic transition is shown by the excitation profile.

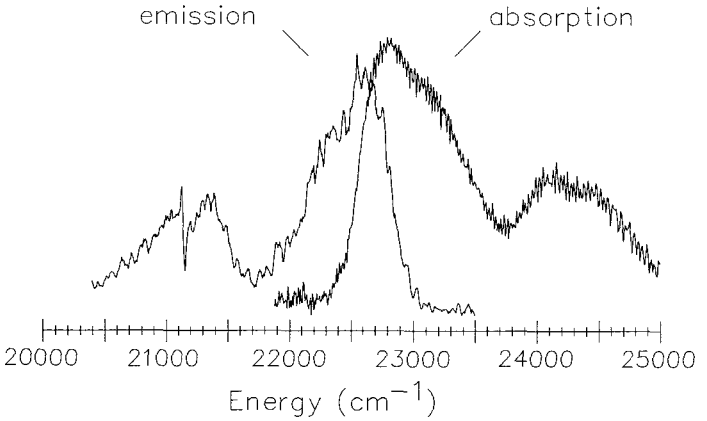

Figure 20. Absorption and emission spectra of perylene doped PMMA at 2 K.

Downloaded At: 17:36 21 January 2011

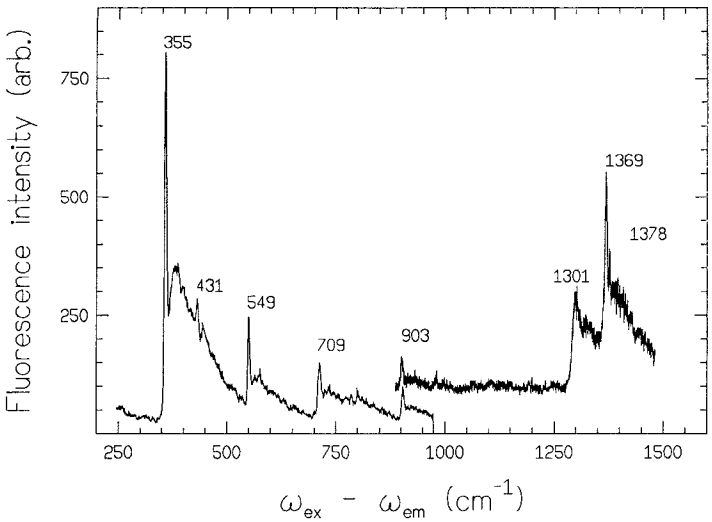

Figure 21. Fluorescence line narrowed spectrum of perylene doped PMMA at 2 K.

Downloaded At: 17:36 21 January 2011

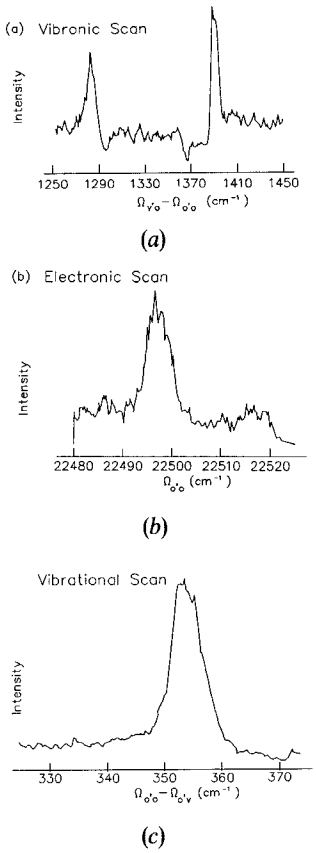

Figure 22. MENS spectra of perylene doped PMMA at 2 K: (*a*) is a vibronic scan with the electronic and vibrational resonances fixed; (*b*) is an electronic scan with the vibrational and vibronic resonances fixed; (*c*) is a vibrational scan with the electronic and vibronic resonances fixed.

inhomogeneous broadening in figure 20. In particular, one can resolve the 1301, 1369 and 1378 cm^{-1} vibrational modes that appear as a broad band in figure 20.

The line-narrowed MENS spectra of the same sample are shown in figure 22 [55]. The top spectrum shows a line-narrowed vibronic scan ($\Omega_{v'o}$ scanned) with $\Omega_{o'o}$ set at 22500 cm^{-1}, on the red side of the electronic absorption band. The vibrational resonance was fixed on the 354·7 cm^{-1} ($\Omega_{o'o}-\Omega_{o'v}=354{\cdot}7$) fundamental. Two vibronic features are seen at 1295 and 1394 cm^{-1}. There is also a dispersive feature in the background at the position of the vibrational transitions at 1369 cm^{-1}. This feature is attributed to a doubly resonant MEPS process (see figure 2) where the resonances correspond to an electronic resonance with sites at $\Omega_{v'o}=22500+1369\,cm^{-1}$ and a vibrational resonance at $\Omega_{v'o}-\Omega_{o'o}=1369\,cm^{-1}$.

Vibronic features are often seen in CARS spectra and are attributed to excited state CARS with resonant enhancement from higher electronic states [73–75]. It is important to verify that the line-narrowed MENS features in figure 22 are caused by the nonlinear line-narrowing mechanism described in the theory section. The characteristic feature of the line-narrowing mechanism is the dependence on all three resonances. This dependence was checked by performing electronic and vibrational scans with the vibronic resonance held constant [55]. The lower two spectra in figure 22 show the electronic and vibrational scans, respectively. In each case, there are sharp peaks at the expected positions that confirm that the line narrowed features are the result of triple resonances with particular sites within the inhomogeneously broadened electronic and vibronic bands.

The same experiments were performed using multiresonant CARS [76]. The CARS spectra also showed the same line-narrowed features as the MENS experiments. They also showed the same dependencies on the electronic and vibrational resonances confirming that the narrow features were not associated with excited state CARS with resonance enhancement from higher electronic states. The narrowing of the vibronic features is attributed to the higher order nonlinear mixing processes described in the theory section.

The linewidths achieved in these experiments were either limited by the lasers or by the homogeneous broadening of the short-lived vibronic states. One would also expect that accidental degeneracy would limit the linewidths. Unlike hole burning experiments or resonant fluorescence line narrowing experiments, the four-wave mixing methods described involve site selection of one state and probing of a different state. This approach cannot give as narrow an ultimate width because the broadening effects on different states are not necessarily identical. This leads to the accidental degeneracy that has limited nonresonant fluorescence line-narrowing experiments.

It would be interesting to pursue the CARS line-narrowing experiments at lower laser intensities in order to eliminate the line-narrowing effects. These experiments were attempted but failed because the CARS signals could not be observed at the low pulse energies that would be required to eliminate saturation effects [53]. The lowest pulse energy that could be achieved without loosing the CARS signal was 20 nJ (or 7 $kW\,cm^{-2}$ laser intensity).

6. Conclusions

Multiply resonant coherent four-wave mixing (CFWM) offers a high degree of spectral selectivity in a molecular measurement because of its unique dependence on a multiplicity of resonances. In the experiments described in this review, the resonances were used for component and mode selection. The nonlinear spectra are simplified by

Downloaded At: 17:36 21 January 2011

the elimination of spectral congestion and the resolution can be improved dramatically by the line-narrowing in inhomogeneously broadened media.

Mode selectivity is a particularly unique capability for CFWM. It allows one to study the relationships between vibrational and vibronic modes. It also offers a method to observe weak or overlapped modes that would be missed in spectroscopic experiments based on single resonances. These capabilities represent important additions to the previously demonstrated capabilities of CFWM, namely freedom from quenching interference, rapid time response, good spatial discrimination, directional and coherent output signal, and fluorescence rejection capabilities.

References

[1] BEGLEY, R. F., HARVEY, A. B., and BYER, R. L., 1974, *Appl. Phys. Lett.*, **25,** 387.
[2] LOTEM, H., 1983, *J. chem. Phys.*, **79,** 2177.
[3] FELKER, P. M., and HARTLAND, G. V., 1987, *Chem. Phys. Lett.*, **134,** 503.
[4] ECKBRETH, A. C., 1978, *Appl. Phys.*, **32,** 421.
[5] LAUFER, G., MILES, R. B., and SANTAVICCA, D., 1979, *Optics Commun.*, **31,** 242.
[6] CHABAY, I., KLAUMINZER, G. K., and HUDSON, B. S., 1976, *Appl. Phys. Lett.*, **28,** 27.
[7] KAMGA, F. M., and SCEATS, M. G., 1980, *Optics Lett.*, **5,** 126.
[8] TOLLES, W. M., NIBLER, J. W., MCDONALD, J. R., and HARVEY, A. B., 1977, *Appl. Spectrosc.*, **31,** 253.
[9] TOLLES, W. M., and TURNER, R. D., 1977, *Appl. Spectrosc.*, **31,** 96.
[10] WRIGHT, J. C., 1982, *Applications of Lasers to Chemical Problems*, edited by T. R. Evans (New York: John Wiley), p. 116.
[11] NIBLER, J. W., and YANG, J. J., 1987, *Ann. Rev. phys. Chem.*, **38,** 349.
[12] TARAN, J. P., 1985, *Analytical Laser Spectroscopy*, edited by S. Martellucci and A. N. Chester (New York: Plenum Press), p. 51.
[13] MOORE, D. S., SCHMIDT, S. C., and SHANER, J. W., 1983, *Phys. Rev. Lett.*, **50,** 1819.
[14] DECOLA, P. L., ANDREWS, J. R., HOCHSTRASSER, R. M., and TROMMSDORFF, H. P., 1980, *J. chem. Phys.*, **73,** 4695.
[15] ANDREWS, J. R., and HOCHSTRASSER, R. M., 1981, *Chem. Phys. Lett.*, **82,** 381.
[16] ANDREWS, J. R., HOCHSTRASSER, R. M., and TROMMSDORFF, H. P., 1981, *Chem. Phys.*, **62,** 87.
[17] ANDREWS, J. R., and HOCHSTRASSER, R. M., 1981, *Chem. Phys. Lett.*, **83,** 427.
[18] CHANG, T. C., JOHNSON, C. K., and SMALL, G. J., 1985, *J. phys. Chem.*, **89,** 2984.
[19] CHANG, T. C., and SMALL, G. J., 1985, *Chem. Phys.*, **99,** 479.
[20] ATTAL-TRETOUT, B., BERLEMONT, P., and TARAN, J. P., 1990, *Molec. Phys.*, **70,** 1.
[21] LEVINSKY, H., and WIERSMA, D. A., 1982, *Chem. Phys. Lett.*, **92,** 24.
[22] WRIGHT, J. C., CARLSON, R. J., RIEBE, M. T., STEEHLER, J. K., NGUYEN, D. C., LEE, S. H., PRICE, B. B., and HURST, G. B., 1989, *Raman Spectroscopy: Sixty Years On, Vibrational Spectra and Structure*, volume 17B, edited by H. D. Bist, J. R. Durig and J. F. Sullivan, (Amsterdam: Elsevier), p. 123.
[23] WRIGHT, J. C., TALLANT, D. R., GUSTAFSON, F. J., JOHNSTON, M. V., MILLER, M. P., MOORE, D. S., PORTER, L. C., and AKSE, J. R., 1979, *Angew. Chem. Int. Ed. Engl.*, **18,** 738.
[24] SZABO, A., 1970, *Phys. Rev. Lett.*, **25,** 924.
[25] EBERLY, J. H., MCGOLGIN, W. C., KAWAOKA, K., and MARCHETTI, A. P., 1974, *Nature*, **251,** 215.
[26] MARCHETTI, A. P., MCGOLGIN, W. C., and EBERLY, J. H., 1975, *Phys. Rev. Lett.*, **35,** 387.
[27] ABRAM, I. I., AUERBACH, R. A., BIRGE, R. R., KOHLER, B. E., and STEVENSON, J. M., 1975, *J. chem. Phys.*, **63,** 2473.
[28] HOCHSTRASSER, R. M., and NYI, C. A., 1979, *J. chem. Phys.*, **70,** 1112.
[29] WRIGHT, J. C., 1981, *Lasers in Chemical Analysis*, edited by G. M. Hieftje, J. C. Travis and F. E. Lytle (Clifton, NJ: Humana Press), p. 77.
[30] ZIEGLER, L. D., 1990, *J. Raman Spectrosc*, **21,** 769.
[31] CHEN, C. K., HEINZ, T. F., RICARD, D., and SHEN, Y. R., 1981, *Chem. Phys. Lett.*, **83,** 455.
[32] BLOEMBERGEN, N., LOTEM, H., and LYNCH, R. T., 1978, *Indian J. pure appl. Phys.*, **16,** 151.
[33] DRUET, S. A. J., TARAN, J. P., and BORDÉ, C. J., 1979, *J. Phys., Paris*, **40,** 819.
[34] OUDAR, J. L., and SHEN, Y. R., 1980, *Phys. Rev.* A, **22,** 1141.

Downloaded At: 17:36 21 January 2011

[35] BORDÉ, C. J., 1983, in *Advances in Laser Spectroscopy*, edited by F. T. Arecchi, F. Strumia and H. Walther (New York: Plenum Press), p. 1.
[36] CARLSON, R. J., and WRIGHT, J. C., 1989, *Phys. Rev.* A, **40,** 5092.
[37] HENDERSON, G., 1980, *Am. J. Phys.*, **48,** 604.
[38] DICK, B., and HOCHSTRASSER, R. M., 1983, *Chem. Phys.*, **75,** 133.
[39] YEE, S. Y., and GUSTAFSON, T. K., 1977, *Phys. Rev.* A, **18,** 1597.
[40] YEE, S. Y., GUSTAFSON, Y. K., DRUET, S. A. J., and TARAN, J. P., 1977, *Optics Commun.*, **23,** 1.
[41] BOZIO, R., DECOLA, P. L., and HOCHSTRASSER, R. M., 1983, in *Time Resolved Vibrational Spectroscopy*, edited by G. H. Atkinson (New York: Academic Press), p. 335.
[42] HOCHSTRASSER, R. M., and TROMMSDORFF, H. P., 1983, *Acc. Chem. Res.*, **16,** 376.
[43] LEE, D., and ALBRECHT, A. C., 1985, in *Advances in Infrared and Raman Spectroscopy*, edited by R. J. H. Clark and R. E. Hester (New York: John Wiley).
[44] MUKAMEL, S., 1982, *Phys. Rev.*, **93,** 1.
[45] MUKAMEL, S., 1983, *Phys. Rev.* A, **28,** 3480.
[46] DRUET, S. A. J., ATTAL, B., GUSTAFSON, T. K., and TARAN, J. P., 1978, *Phys. Rev.* A, **18,** 1529.
[47] NGUYEN, D. C., and WRIGHT, J. C., 1985, *Chem. Phys. Lett.*, **117,** 224.
[48] STEEHLER, J. K., and WRIGHT, J. C., 1985, *J. chem. Phys.*, **83,** 3200.
[49] PRIOR, Y., BOGDAN, A. R., DAGENAIS, M., and BLOEMBERGEN, N., 1981, *Phys. Rev. Lett.*, **46,** 111.
[50] OUELLETTE, F., and DENARIEZ-ROBERGE, M. M., 1982, *Can. J. Phys.*, **60,** 877.
[51] OUELLETTE, F., and DENARIEZ-ROBERGE, M. M., 1982, *Can. J. Phys.*, **60,** 1477.
[52] CARLSON, R. J., and WRIGHT, J. C., 1987, *Chem. Phys. Lett.*, **140,** 101.
[53] RIEBE, M. T., and WRIGHT, J. C., 1988, *J. chem. Phys.*, **88,** 2981.
[54] CARLSON, R. J., 1988, Ph.D. thesis, University of Wisconsin–Madison, available from University Microfilms, Ann Arbor, MI.
[55] HURST, G. B., and WRIGHT, J. C., 1991, *J. chem. Phys.*, **95,** 1479.
[56] CARLSON, R. J., and WRIGHT, J. C., 1989, *Appl. Spectrosc.*, **43,** 1195.
[57] DUTTA, P. K., and SPIRO, T. G., 1978, *J. chem. Phys.*, **69,** 2119.
[58] DUTTA, P. K., DALLINGER, R., and SPIRO, T. G., 1980, *J. chem. Phys.*, **73,** 3580.
[59] STEEHLER, J. K., and WRIGHT, J. C., 1985, *J. chem. Phys.*, **83,** 3188.
[60] DESIDERIO, R. A., and HUDSON, B. S., 1985, *Chem. Phys. Lett.*, **61,** 445.
[61] DICK, B., and HOCHSTRASSER, R. M., 1983, *J. chem. Phys.*, **78,** 3398.
[62] LEE, S. H., STEEHLER, J. K., NGUYEN, D. C., and WRIGHT, J. C., 1985, *Appl. Spectrosc.*, **39,** 243.
[63] CARLSON, R. J., and WRIGHT, J. C., 1990, *J. molec. Spect.*, **143,** 1.
[64] CARLSON, R. J., NGUYEN, D. C., and WRIGHT, J. C., 1990, *J. chem. Phys.*, **92,** 1538.
[65] CARLSON, R. J., and WRIGHT, J. C., 1990, *J. chem. Phys.*, **92,** 5186.
[66] CARLSON, R. J., and WRIGHT, J. C., 1990, *J. chem. Phys.*, **93,** 2205.
[67] RIEBE, M. T., 1987, Ph.D. thesis, University of Wisconsin–Madison, available from University Microfilms, Ann Arbor, MI.
[68] PRICE, B. B., and WRIGHT, J. C., 1990, *Anal. Chem.*, **62,** 1989.
[69] STEEHLER, J. K., and WRIGHT, J. C., 1985, *Appl. Spectrosc.*, **39,** 451.
[70] NGUYEN, D. C., and WRIGHT, J. C., 1985, *Appl. Spectrosc.*, **39,** 230.
[71] CARLSON, R. J., and WRIGHT, J. C., 1991, *Anal. Chem.*, **63,** 1449.
[72] RIEBE, M. T., and WRIGHT, J. C., 1987, *Chem. Phys. Lett.*, **138,** 165.
[73] LAU, A., KONIG, R., and WEIGMANN, H. J., 1980, *Chem. Phys. Lett.*, **69,** 87.
[74] MATSUBARA, S., and TAKAHASHI, H., 1984, *Chem. Phys. Lett.*, **108,** 475.
[75] APANASEVICH, P. A., KVACH, V. V., and ORLOVICH, V. A., 1989, *J. Raman Spectrosc.*, **20,** 125.
[76] HURST, G. B., and WRIGHT, J. C., 1991, *J. chem. Phys.* (to be published).

Downloaded At: 17:36 21 January 2011